Article
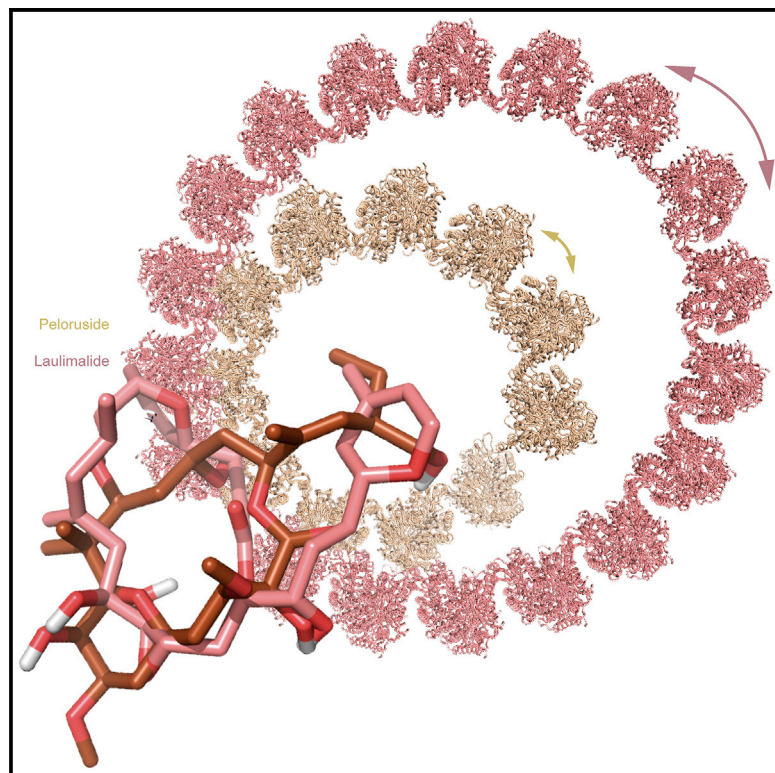
# Chemical modulation of microtubule structure through the laulimalide/peloruside site

## Graphical abstract

## Authors

Juan Estévez-Gallego,
Beatriz Álvarez-Bernad, Benet Pera, ...,
Johan Van der Eycken,
J. Fernando Díaz, María Ángela Oliva

## Correspondence

marian@cib.csic.es

## In brief

Microtubules are linked to cancer growth and are a chemotherapy target. Estévez-Gallego et al. provide insights into the mechanism of drugs targeting the stabilization pocket known as laulimalide site in microtubules. These findings will help to target microtubules also in other diseases and to unravel the relationship of microtubule structure and neurotoxicity.

## Highlights

- Chemotypes targeting the laulimalide site do not induce microtubule lattice expansion

- Microtubule stabilization through the laulimalide site involves only lateral contacts

- Variations of chemotypes targeting the laulimalide site alter inter-protofilament angle

CellPress

**Article**

# Chemical modulation of microtubule structure through the laulimalide/peloruside site

Juan Estévez-Gallego,[1] Beatriz Álvarez-Bernad,[1] Benet Pera,[1] Christoph Wullschleger,[2] Olivier Raes,[3] Dirk Menche,[4] Juan Carlos Martínez,[5] Daniel Lucena-Agell,[1] Andrea E. Prota,[6] Francesca Bonato,[1] Katja Bargsten,[6] Jelle Cornelus,[3] Juan Francisco Giménez-Abián,[1] Peter Northcote,[7] Michel O. Steinmetz,[6,8] Shinji Kamimura,[9] Karl-Heinz Altmann,[2] Ian Paterson,[4] Federico Gago,[10] Johan Van der Eycken,[3] J. Fernando Díaz,[1] and María Ángela Oliva[1,11,*]

[1]Centro de Investigaciones Biológicas Margarita Salas - Consejo Superior de Investigaciones Científicas, Madrid 28040, Spain
[2]Department of Chemistry and Applied Biosciences, Institute of Pharmaceutical Sciences - ETH Zurich, Zürich 8093, Switzerland
[3]Department of Organic and Macromolecular Chemistry, Ghent University, Gent 9000, Belgium
[4]Yusuf Hamied Department of Chemistry, University of Cambridge, Cambridge CB2 1EW, UK
[5]ALBA Synchrotron, CELLS, Cerdanyola del Vallés 08290, Spain
[6]Laboratory of Biomolecular Research, Division of Biology and Chemistry, Paul Scherrer Institut, Villigen 5232, Switzerland
[7]Ferrier Research Institute, University of Wellington, Lower Hutt 5010, New Zealand
[8]University of Basel, Biozentrum, Basel 4056, Switzerland
[9]Department of Biological Sciences, Faculty of Science and Engineering, Chuo University, Tokyo 192-0393, Japan
[10]Department of Biomedical Sciences and Associated Unit IQM-UAH, Universidad de Alcalá, Alcalá de Henares 28805, Spain
[11]lead contact
*Correspondence: marian@cib.csic.es
https://doi.org/10.1016/j.str.2022.11.006

**SUMMARY**

Taxanes are microtubule-stabilizing agents used in the treatment of many solid tumors, but they often involve side effects affecting the peripheral nervous system. It has been proposed that this could be related to structural modifications on the filament upon drug binding. Alternatively, laulimalide and peloruside bind to a different site also inducing stabilization, but they have not been exploited in clinics. Here, we use a combination of the parental natural compounds and derived analogs to unravel the stabilization mechanism through this site. These drugs settle lateral interactions without engaging the M loop, which is part of the key and lock involved in the inter-protofilament contacts. Importantly, these drugs can modulate the angle between protofilaments, producing microtubules of different diameters. Among the compounds studied, we have found some showing low cytotoxicity and able to induce stabilization without compromising microtubule native structure. This opens the window of new applications for microtubule-stabilizing agents beyond cancer treatment.

## INTRODUCTION

Microtubules (MTs) are long, relatively stiff helical filaments composed of αβ-tubulin heterodimers. Given the importance of MTs for cell homeostasis, the natural evolutionary pressure has led to the emergence of a large number of compounds that can interfere with MT regulation by targeting up to seven druggable sites in tubulin, which are named after their prototypical ligand: colchicine,[1,2] taxane,[3,4] vinblastine,[5,6] peloruside/laulimalide,[7–9] pironetin,[10–12] maytansin,[13–15] and gatorbulin.[16] These compounds, which can be natural products, semisynthetic derivates of natural products, or synthetics, are pharmacologically classified as MT-targeting agents (MTAs). Depending on the overall effect on MT polymerization, they are divided into two families: the MT-stabilizing agents (MSAs) and the MT-destabilizing agents.[17]

MSAs—and particularly compounds binding to the taxane site—are some of the most successfully employed drugs in cancer chemotherapy.[18,19] Among them, paclitaxel (Taxol, PTX), docetaxel (Taxotere), cabazitaxel (Jevtana), and ixabepilone (Ixempra) are approved drugs for the clinical management of several cancers. Despite the great success of these drugs for the treatment of ovarian, lung, and breast cancer, in addition to Kaposi sarcomas, their low solubility, toxicity, and drug resistance limit their use. Two main mechanisms of taxane drug resistance have been proposed: overexpression of the P-gp efflux pumps[20] and upregulation of the expression of less-sensitive β-tubulin isotypes, such as βIII.[21,22] There is an additional drawback of these drugs related to the appearance of side effects. Among them, peripheral neurotoxicity (damage or destruction of peripheral nerves) is the most limiting for the successful treatment of patients.[23] Very likely effects on MTs trafficking mediated by kinesins and dyneins[24] are involved, because this is essential in neuronal function. However, the underlying mechanisms are not yet clear, and it is not intuitive why MSAs, which virtually preserve the scaffold and road functions of MTs for intracellular long
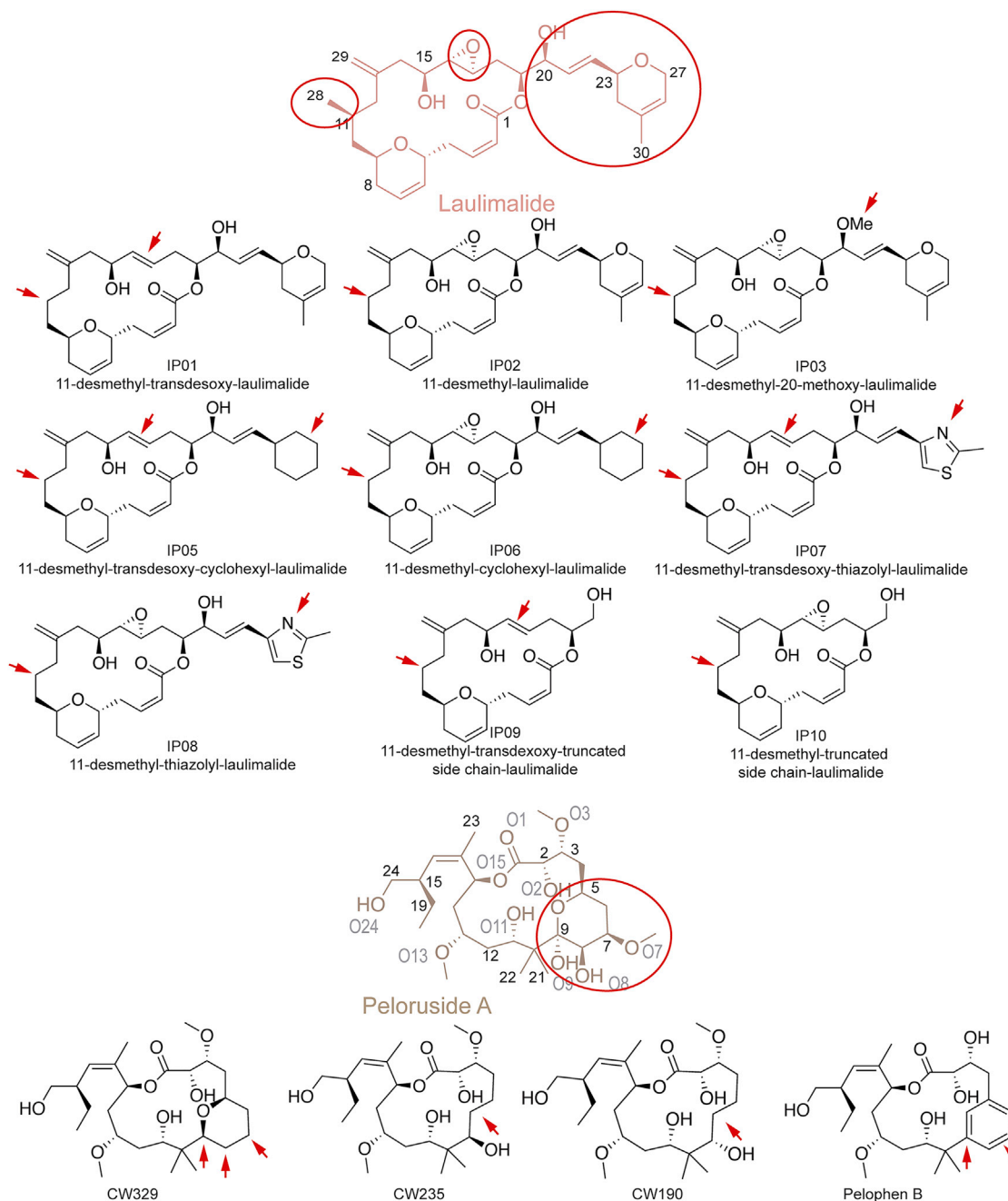
Figure 1. Chemical structure of the LP site targeting compounds employed in this study

distances transport, should have a detrimental impact on neuronal function. It has been proposed recently that neurotoxicity is caused by the mechanism itself of taxane site-induced MT stabilization,[19,25] which is based on modification of the longitudinal and lateral tubulin lattice contacts.[26–28] These modifications of the MT structure could disrupt the recognition patterns for regulatory MT-associated proteins (MAPs) and motor proteins, thus perturbing the neural function.[29]

The laulimalide/peloruside (LP) site was initially described as being targeted by two marine natural products, namely laulima-

lide (LAU) and peloruside A (PLA, Figure 1). It is located on the MT surface between neighboring protofilaments (PFs)[9] rather than in the lumen, as is the taxane site. LAU is a macrocyclic lactone isolated from the sponge *Cacospongia mycofijensis* that promotes tubulin assembly into MTs. It is about 100-fold more potent than PTX against P-gp overexpressing cell lines,[30] but unfortunately it exhibits low antitumor potency and severe toxicity, which has limited interest in its clinical or even preclinical development.[31] PLA, originally isolated from the sponge *Mycale henstcheli*,[32] is a macrocyclic lactone like LAU, and similar to it, PLA stabilizes

MTs through lateral inter-PF contacts without inducing axial expansion,[8,27] and it forces cell-cycle arrest at the $G_2/M$ phase.[33] Otherwise, this compound shows higher antitumor potency and lower toxicity than LAU.[34,35] Furthermore, contrary to taxanes, PLA produces MT stabilization in tau-overexpressing neuroblastoma cells without being affected by higher levels of tau protein.[36] The main drawbacks of LAU and PLA are the scarcity of natural material, which limits their availability, and the complexity and low product yield of their total syntheses.[37–40]

Here, we have investigated LP site chemotypes including structurally simplified PLA analogs. We aimed to understand the interplay between these compounds' binding affinity to MTs, their cytotoxicity, and their structural effect on the MT lattice. We have found that the MT stabilization exerted through the LP site is clearly distinct from the one arising from occupancy of the taxane-binding site and that each chemotype shows distinctive features. Unexpectedly, we have discovered that LAU binding to tubulin is entropy driven and favors the formation of MTs with a compact lattice but higher number of protofilaments (PF) and, hence, an increased diameter. Furthermore, small modifications of LAU seriously affect its binding affinity and the effect on the MT, which hampers the development of successful analogs. In addition, we noticed that PLA is an optimized molecule in terms of binding affinity and cytotoxicity, but modifications on the tetrahydropyran ring are tolerated, and synthesis can be simplified while retaining tubulin binding and effective cellular effects. PLA induces the formation of smaller MTs similar to those grown in the presence of PTX, but modifications of the tetrahydropyran ring confer variability on lateral interactions between PFs that is similar to those encountered in non-stabilized MTs. Together, our results show how the structure of the MT is modified by MT-binding ligands through lateral interactions, and they highlight new options for the pharmacological stabilization of MTs without compromising the natural architecture of these filaments in cells, thus opening the window for novel clinical applications of these MTAs.

## RESULTS

### Distinct effects on the lattice of ligand-stabilized microtubules depending on the targeted site

MTs are GDP-bound filaments bearing a differential GTP cap at their ends. We previously used and validated X-ray fiber diffraction of shear-flow aligned MTs to characterize the main structural features of MTs according to the nucleotide bound state.[25] This technique allows us to define MT parameters from the equatorial signals (lateral features such as the radius, average number of PFs, and inter-PF distance) and from the meridional ones (with accurate measurements of the axial average monomer length, Figure S1). The 1-nm band (the 4th armonic of the layer line corresponding to the helical rise of the MT) allows measurement with high precision (sub-Å resolution) of the axial spacing. When the 1-nm band peak locates at $\sim$6.20 nm$^{-1}$, the axial spacing between consecutive subunits is shorter, and therefore, the MT lattice is in a "compact" state (GDP-bound). If this band locates at $\sim$6.02 nm$^{-1}$, then longitudinal distances between $\alpha$- and $\beta$-tubulin are larger, which is related to an "expanded" state that is typical of MTs assembled with the non-hydrolysable GTP analog GMPCPP.[25] Here, we have analyzed the effect of LAU

and PLA chemotypes on GDP-bound MTs (compact lattice) and GMPCPP-bound MTs (expanded lattice) to understand the underlying mechanism of the stabilization through the LP site compared with the one through the taxane site (Table S1, Figure 2).

We first sought to define the main features of MTs stabilized with LAU and PLA compared with non-stabilized MTs and PTX stabilized (all on the GDP-bound state). Both non-stabilized and MTs stabilized through the LP site (LAU- and PLA-MTs) display compact longitudinal lattices (Figure 2A), which clearly oppose the characteristic expanded lattice of PTX-MTs.[25,27] However, the stabilization through the LP site highlighted some differences with non-stabilized MTs regarding the lateral arrangements (Figure 2B). LAU-stabilized MTs have a larger average radius than drug-free MTs (12.21 vs. 11.42 nm). Because the average inter-PF distance remains similar (5.50 nm in LAU-MTs and 5.46 nm in non-stabilized MTs), the increase in diameter in the presence of the drug appears to be related to the accommodation of one more PF, on average, ($\sim$14-PFs vs. $\sim$13-PF, Table S1). In fact, the analysis of MT sub-populations in solution shows that LAU-MTs include 8% of 10-PF, 7% of 11-PF, 12% of 13-PF, 27% of 14-PF, 32% of 15-PF, and 13% of 16-PF (with no subpopulation of 12-PF), whereas non-stabilized MTs include 8% of 11-PF, 22% of 12-PF, 40% of 13-PF, and 30% of 14-PF and do not include 15- nor 16-PF (Figure 2C). In contrast, the stabilization with PLA significantly decreases the average radius compared with non-stabilized MTs (10.84 vs. 11.42 nm), which is similar to that found in PTX-MTs (10.87 nm). However, different from PTX-MTs, PLA increases the average inter-PF distance (5.71 vs. 5.45 nm), which denotes that PLA binding might result in a slight modification of lateral interactions and a reduced number of PFs (Table S1). Accordingly, we found that the PLA-MTs population analyzed included 5% of 10-PF, 31% of 11-PF, 43% of 12-PF, 20% of 13-PF, and 1% of 14-PF, whereas PTX-MTs included 2% of 10-PF, 28% of 11-PF, 29% of 12-PF, 30% of 13-PF, and 11% of 14-PF (Figure 2C). In conclusion, MTs stabilized through the LP site do not display any noticeable differences in axial spacing compared with non-stabilized MTs as opposed to PTX. In stark contrast, our results do highlight chemotype-dependent differences in the lateral spacing, with bending angles between neighbor PFs that vary in opposite directions. Thus, the presence of LAU allows an increase in the number of PFs that make up MTs with an increased diameter, whereas PLA binding results in MTs with a lower number of PFs.

In addition, to determine the possibility of any allosteric effect between the stabilization pocket and the nucleotide-binding site, we further studied the MSA-stabilized MTs grown in the presence of GMPCPP. It is known that this GTP analog does not generate any significant change in lateral contacts between PFs while inducing axial expansion of MTs[25,41] (Table S1). We found that PLA did not override GMPCPP-induced axial expansion (Table S1, Figure 2D), further supporting the lack of effect on the longitudinal contacts along the MT. Instead, in the presence of LAU, the position of the 1-nm band was halfway between compact and expanded lattice (at 6.11 nm$^{-1}$; Figure 2D, inset). We relate this result to an equilibrium between mixed populations of compact vs. expanded MT lattices in solution rather than to the existence of an intermediate expansion state
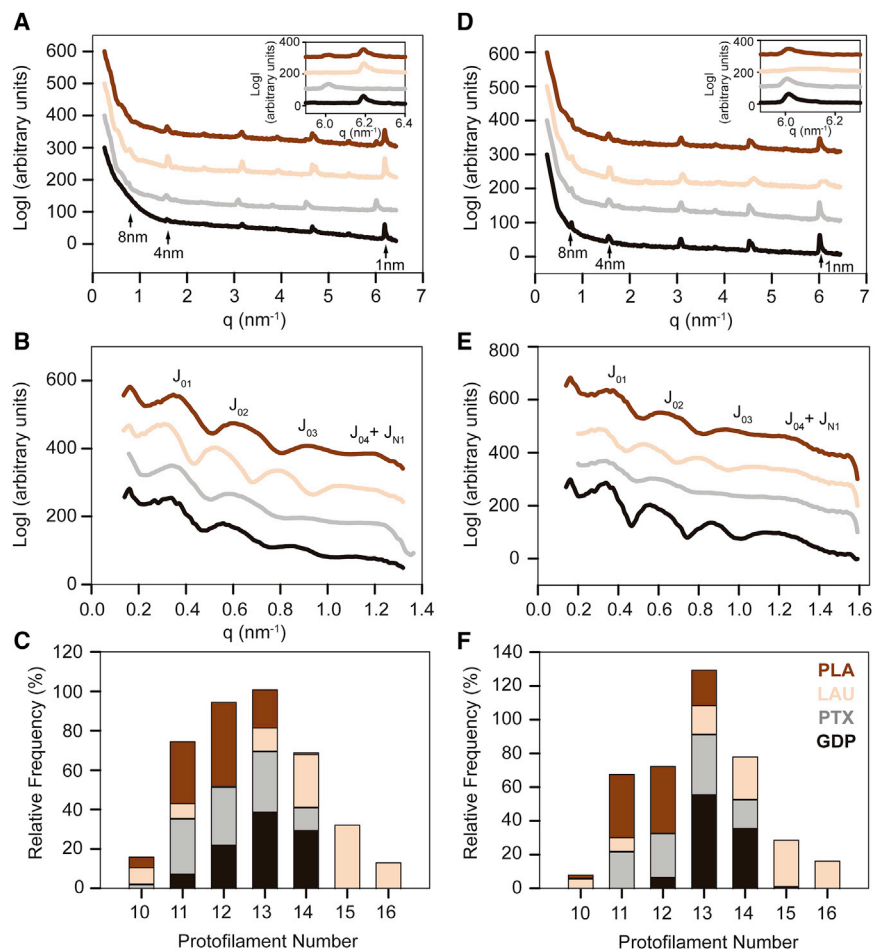
**Figure 2. Fiber diffraction of stabilized MTs**

Control MTs (black), PTX-MTs (gray), LAU-MTs (salmon), PLA-MTs (brown).

(A–C) GDP-bound MTs and (D and E) GMPCPP-bound MTs. (A and D) Meridional intensity profiles. The inset shows the best fit of 1-nm band experimental intensities in a Lorentzian normal distribution, highlighting positional differences between all tested conditions (peaks maxima, arrows). (B and E) Equatorial intensity patterns showing the corresponding Bessel function from $J_{01}$ to $J_{04} + J_{N1}$. (C and F) Estimation of the number of PFs per MT and percentage of each subpopulation within the solution from fiber diffraction experiments.

See also Figures S1 and S2 and Table S1.

vided information about the opposite wedge effect of the ligands at the β:β interface, whereas the latter allowed us to study and compare the ligand-protein interactions at a binding site that resembles the conformationally constrained MT environment.

Lateral interactions between PFs are flexible enough to accommodate a wide range of bending angles, as shown by previous normal mode analyses on MTs (for which stretching, bending, torsional, and breathing models have been independently described).[43,44] Additionally, our calculations on two laterally associated β subunits reveal the opening/closing motions conductive t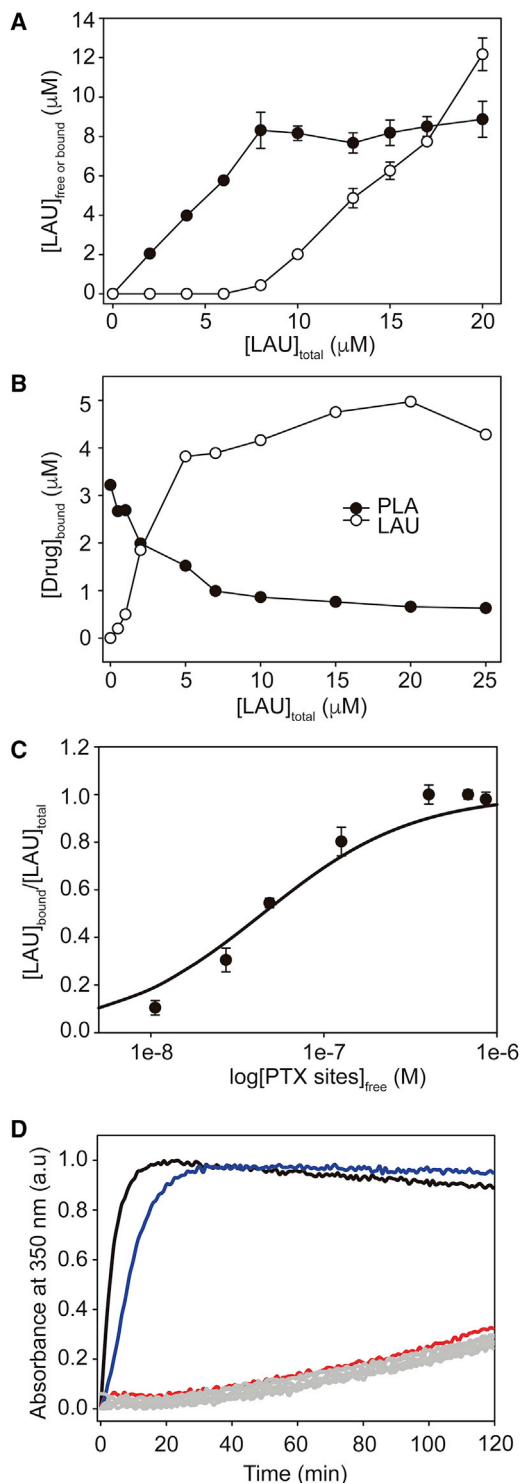o MTs with varying number of PFs (Video S1). This behavior nicely accounts for our fiber diffraction data, which show distinct variations in the average number or PFs in the presence of each compound: 12-PFs for PLA-MTs vs. 14-PFs for LAU-MTSs (Figure S2C). Remarkably, this difference can arise from a $\beta_1$:$\beta_{1'}$ angular difference of as little as 4.3°, and as much as 9° if comparing the 30% subpopulation of PLA-MTs of 11-PFs and the 32% subpopulation of LAU-MTs of 15-PFs.

As expected, LAU and PLA molecules were subjected to larger fluctuations and gave rise to less favorable interactions energies when bound at the exposed site of the MT than when bound at the interfacial site. Both LAU and PLA are highly preorganized macrocycles that bury a large percentage of non-polar surface upon binding to β-tubulin, hence contributing to a hydrophobic effect that is proportional to the number of H-C bonds that are excluded from water,[45] while simultaneously engaging a number of optimally oriented oxygen atoms in hydrogen-bonding interactions with residues from both β-tubulin subunits (Figure S2D). In the case of LAU, it is noteworthy that the entropic contribution to the binding free energy (see below) is expected to arise from (1) the geometrically constrained conformation in solution of the compound (i.e., the small number of rotational degrees of freedom minimizes the ligand entropy loss upon binding) and (2) the release of solvent from non-polar surfaces that is not offset by enthalpic penalties,[46] even though at least two of the hydrogen bonds that stabilize the bound ligand are water-

because: (1) the 1-nm band observed is not sharp (Figure S1) and, (2) the fiber diffraction signal recorded in these experiments is the result of the diffraction of all MTs in the sample during a period of time and, thus, an average cue. Therefore, we speculate that LAU could exert some effect through the lattice axial contacts that is not strong enough to fully compact GMPCPP-induced expansion. Importantly, GMPCPP does not affect the overall lateral contacts in MTs stabilized by these MSAs (Figures 2E and 2F), and LAU- and PLA-MTs in the presence of this analog retain a similar radius, average PF number, and inter-PF distance to their GTP-stabilized counterparts. Consequently, these results support the idea that the MTs' stabilization mechanism exerted through the LP site involves only lateral contacts between PFs.

## Laulimalide and peloruside A bind differently to the pocket built between two protofilaments

We used atomistic modeling to further sample the conformational space and analyze the binding of LAU and PLA to the LP site. For this purpose, we simulated (1) a fully solvated ensemble of two laterally associated β subunits (Figure S2A) and (2) a minimalistic representation of a bovine MT consisting of the $\alpha_1$:$\beta_1$:$\alpha_2$ subunits from one PF together with the closely interacting $\alpha_{1'}$:$\beta_{1'}$:$\alpha_{2'}$ subunits from the parallel, neighboring PF, essentially as described previously[42] (Figure S2B). The former complex pro-

mediated, a finding that can be interpreted as leading to an increase in order. However, our analyses of the MD trajectories reveal that these water molecules do not fulfill their whole hydrogen-bonding potential with the ligand-protein complex and can effectively exchange with other water molecules from the bulk solvent. In addition, given the highly charged nature of several interfacial protein residues, it is likely that LAU binding affects the stability of $\beta_1$:$\beta_{1'}$ side-chain:side-chain ion pairs involving E290, D297, K299, and K338 from one subunit and D120′, R123′, K124′, and E127′ from the other subunit across the cleft (i.e., the conformational entropy of some of these side chains would be enhanced upon drug binding; Figure S2E). In fact, both LAU and PLA interact with many common residues at the $\beta_1$: $\beta_{1'}$ lateral interface that belongs to helices H9 and H10 and loops H9-S8 and H10-S9 (Figures S2E and S2F). However, the specific binding energies from $\beta_1$:$\beta_{1'}$ residues vary depending on the compound, which may be related to the differences on the resulting inter-PF accommodated angle found. Importantly, in both complexes, the backbone carbonyl of D120 from the $\beta_{1'}$ subunit acts as a hydrogen bond acceptor for a hydroxyl group from each drug.

### Unique binding energetics of laulimalide to the LP site

We initially used cross-linked stabilized MTs for the biochemical characterization of LAU binding to the LP site because it is known that this pocket is well preserved in those.[33] We found that LAU binds to cross-linked MT with a stoichiometry of 0.83 ± 0.02 (mol of LAU per mol of active PTX binding site; Figure 3A), which is close to the 1:1 stoichiometry observed for the binding of PLA to the same site as well as other MSAs to the taxane-binding site.[33,47,48] Competition assays with 5 μM of cross-linked MT preincubated with 5 μM PLA and 5 μM PTX (used to prevent nonspecific binding to the taxane site) and increasing concentrations of LAU confirmed that LAU and PLA bind to the same site (Figure 3B). Finally, we determined the equilibrium binding constant of LAU by centrifugation assays and found a $K_b$ of $1.9 \pm 0.2 \times 10^7$ M$^{-1}$ at 25°C (Figure 3C), which is roughly one order of magnitude higher than that of PLA.[33] Despite the large errors on the $K_b$ determination inherent to the method, our results showed that the binding constant increased with temperature (Table S2), indicating that LAU binding is entropy driven ($\Delta H > 0$, i.e., the free energy of binding arises from the increase of entropy of the final state).

We next sought to relate the cellular and biochemical effects of these compounds to the binding affinity of this chemotype for the LP site on the basis that binding affinity is an excellent predictor of the cellular effects of taxane site ligands.[49–52] There are extensive studies about the cellular effects of LP site ligands, but little is known about the ligands' structure-affinity relationships apart

**Figure 3. Biochemistry on LAU interaction with cross-linked MTs**
(A) LAU binding stoichiometry to 10 μM MT in buffer GAB with 0.1 mM GTP at 25°C. Concentrations of free LAU (black dots) and bound LAU (white dots).
(B) Competition assay between LAU and PLA in the presence of 5 μM PLA + 5 μM PTX sites and 0, 1, 2, 5, 7, 10, 15, 20, and 25 μM of LAU in GAB with 0.1 mM GTP. Concentration of bound PLA (black dots) and concentration of bound LAU (white dots).

(C) LAU binding isotherm curve, where black dots represent the molar saturation fractions of increasing concentrations of stabilized MTs (noted as PTX binding sites) in the presence of X μM of LAU.
(D) Time-lapse polymerization assays of LAU (black) and its derivatives IP02 (dark blue) and IP01, IP03, and IP05-IP10 (gray-scale) compared with control vehicle (0.5% DMSO, red line). For all sections, results correspond to the average result obtained from three independent experimental replicates. Error bars correspond to the SEM.
See also Table S2.
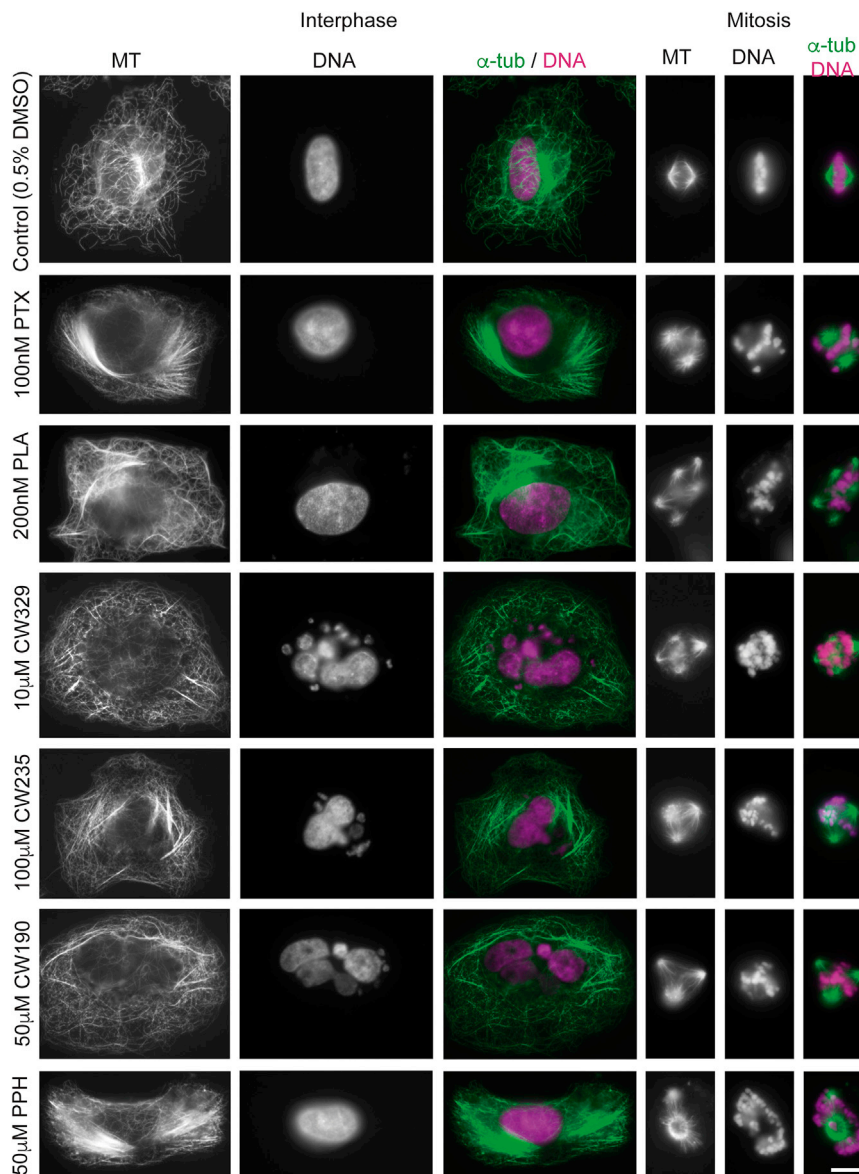
**Figure 4. Effects of PLA analogs in interphase and mitotic cells**

Each row shows α-tubulin immunostaining (DM1A antibody), DNA (DAPI staining), and the merge of the previous ones (tubulin in green and DNA in magenta) of interphase cells (first three columns) and mitotic cells (following three). Top row are control cells treated with 0.5% DMSO (compounds vehicle), where the usual MT network is observed evenly distributed in the interphase cell cytoplasm and denser around the nucleus, whereas a normal bipolar spindle with chromosomes aligned at the metaphase plate is displayed at the mitotic phase. In following rows, 100 nM PTX, 200 nM PLA, 10 μM CW329, 100 μM CW235, 50 μM CW190, and 50 μM PPH treated cells, where a denser micro-tubular network characterize by bundles of MTs is visible in interphase, and a diversity of abnormal mitotic spindles containing misaligned chromosomes are displayed in mitotic cells. All images are shown at the same magnification; scale bar: 10 μm. See also Figures S1–S3 and Tables S1 and S3.

IP01 (5.8 × 10$^4$ M$^{-1}$ at 25°C) and IP06 (2.1 × 10$^4$ M$^{-1}$ at 25°C) displaced IP02, showing 330 times and 900 times lower affinity for the LP site than IP02, whereas the remaining compounds were unable to displace IP02 at any concentration. These results are in good accord with the weak effect observed in the MT assembly assay and further suggest that modifications of the LAU structure seriously impair the effects of the compound in tubulin nucleation, MTs stabilization, and cytotoxicity.
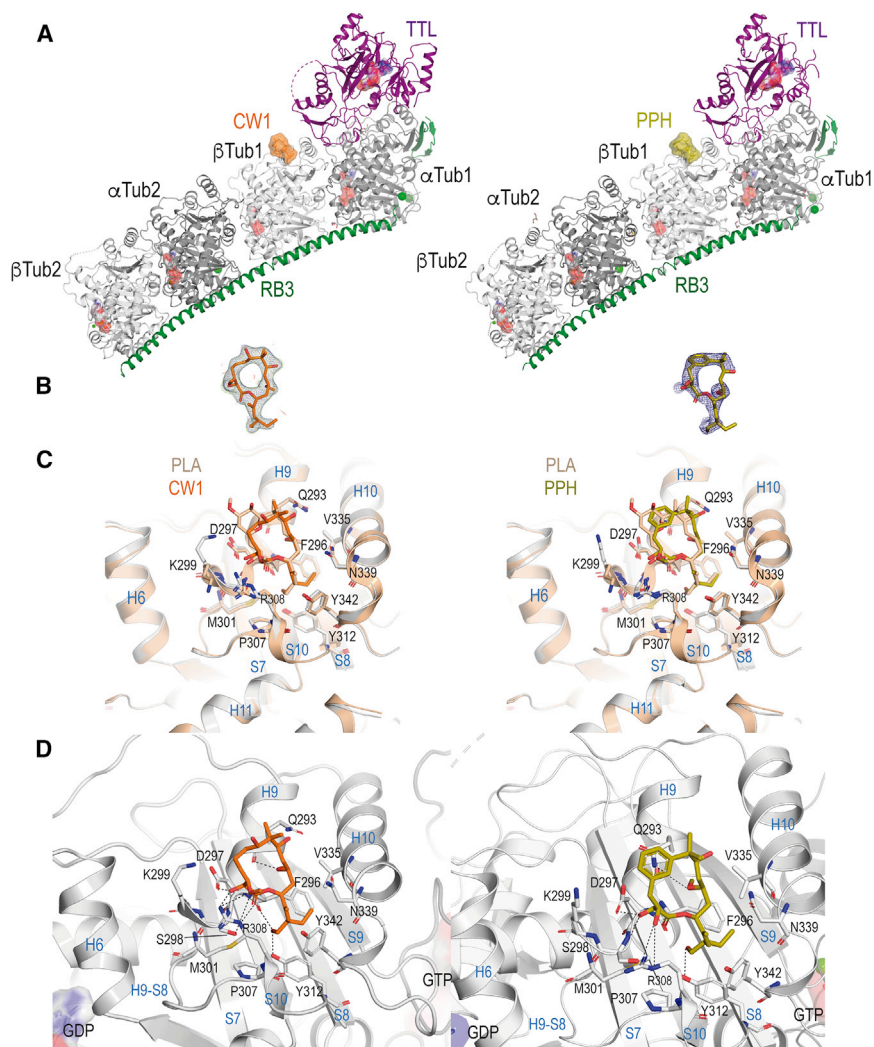
## Peloruside A analogs override drug effect on the MT lattice structure

Based on the binding mode of PLA to β-tubulin,[9] we made a selection of new PLA analogs to explore simplifications of the tetrahydropyran ring that included (1) elimination of the C7 methoxy and the C8 and C9 hydroxy groups (CW329[54]) and (2) removal of the entire tetrahydropyran ring (CW235 and CW190[54]) or replacement of the latter by an aromatic moiety (pe-lophen B [PPH], Figure 1).

We found that all the simplified compounds derived from PLA bound well to the LP site on cross-linked MT at 25°C with binding affinities in the range of 10$^5$ M$^{-1}$ (Table S3), which are one order of magnitude lower than that of the lead compound. This can be related to the overall lower free energy of binding we found in the interaction of tubulin with CW190 and PPH (Figures S2E, S2G, and S2H). The ability of these analogs to induce tubulin nucle-ation upon assembly, measured as critical concentration (Cc), was also lower than that of parental compound, though all PLA analogs effectively decreased tubulin Cc (Table S3). Immunoflu-orescence assays on A549 cells (Figure 4) showed that CW329, CW235, CW190, and PPH induced bundling and

from the influence of the side chain on the ability to induce tubulin assembly and cause cytotoxicity.[53] Therefore, we started from a set of nine LAU derivatives (Figure 1) that we previously evaluated for their ability to stabilize MTs under conditions favoring tubulin assembly (GAB buffer).[53] Here, we have analyzed the ability of LAU (1), IP01 (14), IP02 (2), IP03 (21), IP05 (22), IP06 (4), IP07 (23), IP08 (5), IP09 (9), and IP10 (3) (number in parenthesis is that employed in Paterson et al.[53]) to induce tubulin assembly under non-favorable tubulin assembly conditions (PEDTA buffer). Considering that LAU analogs are able to stabilize MTs (IP01, IP02, and IP06,[53]), we found that only IP02 also induced MT nucleation (Figure 3D). However, IP02's binding affinity for cross-linked MT (2.6 ± 0.4 × 10$^6$ M$^{-1}$ at 25°C) was seven times lower than that of LAU, which is in good accord with the ratio of cytotoxicities observed previously (which are 15 times lower for IP02[53]). We further tried to evaluate the binding constant of all other LAU analogs in a competition assay against IP02. Only

**Figure 5. High-resolution structures of CW190 and PPH in the T₂R-TTL complex**

(A) Overall structure of T₂R-TTL complex in the presence of CW190 (left) and PPH (right), where proteins are in ribbon representation (α-tubulin in gray, β-tubulin in white, TTL in purple, and RB3 in green), and the compounds are represented in surface bound to the LP site of β-tubulin in orange (CW190, left) and dark yellow (PPH, right).

(B) The sigma A weighted 2mFo-DFc (blue) electron density map contoured at 1.0 sigma of CW190 (left) and PPH (right), which are in stick representation.

(C) Comparison of PLA (brown sticks) and CW190 (orange sticks, left) or PPH (dark yellow sticks, right) interaction in the LP site highlighting secondary structure elements of β-tubulin (blue) and main residues involved in the interaction (sticks).

(D) Hydrogen bonding of CW190 (left) and PPH (right) at the LP site in β-tubulin.

See also Table S4.

hyperstabilization of MTs in interphase and aberrant mitoses with multiple poles in metaphase, similar to PLA and PTX. However, the concentration of analogs required to see these effects was between 50 and 500 times higher than that of PLA. In fact, IC₅₀ assays in the human ovarian carcinoma cell line A2780 showed that these ligands had 50–800 times lower cytotoxicities than the parental compound (Table S3). Remarkably, all PLA analogs remained active in A2780AD cells (an MDR line overexpressing P-gp), indicating that—like the parental compound—they are poor substrates for the P-gp detoxification pump.

In order to understand the relevance of the tetrahydropyran ring on the binding affinity to tubulin and the cytotoxicity, we approached structural studies using macromolecular crystallography experiments. To this end, we grew crystals of the T₂R-TTL tubulin complex, which contains two αβ-tubulin heterodimers (T₂), the stathmin-like protein RB3 (R) and the tubulin tyrosine ligase (TTL),[55] and we performed soaking experiments with compounds CW190 and PPH. The structures of the T₂R-TTL-CW190 and T₂R-TTL-PPH complexes refined to 2.00-Å and 2.50-Å resolution, respectively (Table S4). Both analogs bind to the LP site on β-tubulin (chain B in the complexes, Figures 5A and 5B) with a very similar pose as the one

observed for PLA (PDB: 4o4j[9]; Figure 5C). The asymmetric arrangement of the protein chains in the T₂R-TTL tubulin complex creates two different environments of the LP sites on chains B and D, which are not equivalent. There is a crystal contact nearby, which certainly has an impact on that, so it is not surprising that the sites are not equally occupied. The β-tubulin chains containing CW190 and PPH superpose very well with that of the PLA structure with a root-mean-square deviation of 0.278 Å (432 Cα-atoms) and 0.156 Å (395 Cα-atoms), respectively, highlighting that all three compounds are bound to the protein in basically the same conformation.

For CW190, the hydrogen bonds are formed with the side chains of Q293, D297/R308, S298, R308, and Y312, respectively (Figure 5D). Moreover, O11 establishes a water-mediated contact to the backbone carbonyl of Q293. However, this water molecule is less well defined compared with the equivalent water in the PLA structure, where it is further stabilized by the O9 hydroxyl. The main difference between the PLA and the CW190 structures is a flip of the K299 side chain to form a salt bridge with D297, which is facilitated by the absence of the tetrahydropyran ring in CW190 (Figures 5C and 5D). Similar to PLA, we found that PPH retains interactions with the side chains of Q293 and D297, R308 and Y312, and with the main chain of S298 (Figure 5D). Remarkably, Q293 shows a very well-defined density occupying the position of the water molecule in the PLA structure and, hence, a modification of the hydrogen bonding in this alternative conformation (that is established with the O13 of PPH). In these structures, the M loop is not well defined due to the absence of clear densities.

Because these structures did not reveal to what extent the tetrahydropyran ring affects the biochemical and cytotoxicity properties of PLA, we further analyzed the effect of CW190 and PPH

on MT structure by fiber diffraction studies. Both compounds give very clear and accurate signals in both directions (equatorial and meridional, Figures S1 and S3), and similar to PLA or LAU, they do not induce MT axial lattice expansion (Table S1, Figure S3A). However, these PLA analogs also showed differences to the parental compound, and the resulting stabilized MTs displayed structural features closer to those of non-stabilized MTs than to those of stabilized PLA-MTs (Table S1). The compounds induced MTs with a radius of 11.09 nm (CW190) and 11.74 nm (PPH), and the average number of PFs was 12.57 (CW190) and 12.96 (PPH), which is similar to the 11.42-nm radius and 12.91 average PFs of non-stabilized MTs. Similarly, the inter-PF distances measured (5.49 nm for CW190-MTs and 5.64 nm for PPH-MTs) were close to those of non-stabilized MTs (5.50 nm), indicating that MT stabilization by these PLA analogs does not significantly affect the MT structure. We assume this to be due to the hydrogen bond patterns found in our *in silico* analysis of protein-ligand interaction, where neither CW190 nor PPH engages in hydrogen bonds with $\beta_{1'}$ residue D120. In addition, similar to PLA, we found that these analogs are not able to override GMPCPP lattice expansion (Table S1, Figure S3D) and neither does GMPCPP modify the lateral arrangements of MTs stabilized with CW190 or PPH (Table S1, Figure S3E). Our molecular simulations pointed to lateral contacts rather than longitudinal ones as the main stabilization mechanism of LP site binders. In fact, the analysis of the free energy of binding of CW190 and PPH (Figures S2G and S2H) showed that the contribution of individual protein residues is closely similar to that of PLA and LAU, so residues involved in the lateral interaction are those from helices H9 and H10 and loops H9-S8 and H10-S9 hold in $\beta_1$ and H3 in $\beta_{1'}$. These results further support a stabilization mechanism that exclusively involves lateral contacts and that might involve H3-H9/H10 rather than the M loop.

## DISCUSSION

MTs are involved in many essential cellular processes due to their dynamic behavior, their mechanical properties, and their ability to exert forces. The cell controls MT functions through a complex regulatory network formed by a plethora of elements such as the MT organizing centers,[56] MAPs,[57,58] and post-translational modifications that determine the dynamic behavior of MTs and the topology of their surface.[59] Another important factor involved is differential expression of tubulin isotypes.[60] Among the crucial processes exerted by MTs, chromosome segregation (MTs are the main component of the mitotic spindle[61]) and vascularization are the fundamental reasons for MTs being a main target in cancer treatment. The pharmacological intervention mainly focuses on the stabilization or destabilization of these filaments affecting their dynamic behavior and, hence, the ability to produce pushing and pulling forces. However, many drawbacks are associated with currently clinical used drugs that support continuous research aiming to obtain more active and safer compounds. Considering cancer treatment with MSAs, patients face, among other issues, peripheral neurotoxicity that could be related to how taxane site drugs achieve MT stabilization, a mechanism that involves modifications of both axial and lateral contacts.[27] In this work, we have observed that drugs targeting the LP site perform MT stabilization exclusively through lateral

contacts with the interplay between H9 and H10 and loops H9-S8 and H10-S9 in one molecule and H3 in the lateral neighbor. Remarkably, our results show that there is no major intervention at the M loop, which otherwise is a key factor on the formation of lateral contacts,[62] and for the stabilization through the taxane site.[27]

LAU and PLA could be good candidates for cancer treatment, but it is necessary to address their scarce occurrence and the complexity and low yield of their total syntheses. Here, we have shown that LAU is a highly optimized chemotype with an entropy-driven interaction with tubulin. The fact that PLA binding is also weakly exothermic (Table S2) points out the different nature of the interaction compared to ligands of the taxane site, where ligand interaction is an exothermic reaction ($\Delta H < 0$, i.e., the ligand binding provides the free energy to stabilize a given structural state by stabilizing interactions with protein residues). Subtle chemical modifications on LAU such as the demethylation in position C11 (IP2) seriously decrease binding affinity and affect the ability of the compound to induce tubulin nucleation upon assembly. In addition, further changes at the side chain completely abrogate the interaction with MTs. Therefore, we foresee a difficult pathway toward the development of more effective and safer compounds from this chemotype. Similarly, we have found that PLA was a highly optimized chemotype because modifications on the tetrahydropyran ring led to compounds with lower affinity and activity. PLA analogs require an increase in drug concentration of 50- to 500-fold to achieve a similar cellular cytotoxicity as for the parental compound. However, these analogs still interact with tubulin and induce MT stabilization.

Strikingly, the stabilization of the axonal MTs by MSAs could be linked to the symptomatic treatment of some neurodegenerative disorders such as tauopathies. These diseases are characterized by the deposition of tau protein aggregates in the brain. Tau is a MAP enriched in the neuronal axon that plays a fundamental role in the regulation of MT dynamics, acting as an MT-stabilizing factor. It has been proposed that the ultimate Alzheimer's disease molecular mechanism is based on abnormal phosphorylation of tau that produces mislocalization of the protein into the somatodendritic compartment, where it forms beta aggregates.[63] Notice that hyperphosphorylated tau loses its ability to bind tubulin and, thus, the cell suffers from an imbalance in MT dynamic regulation. Hence, the use of MSAs could be a rational pharmacological strategy in the treatment of Alzheimer's disease and other neurodegenerative diseases where MT integrity is compromised.[64,65] MSAs should not affect the static function of MTs, which serve as tracks for the intracellular long-distance transport and the scaffolding behavior. However, the observation of neuronal degeneration induced by treatment with taxane site MSAs in cancer chemotherapy indicates that their use as MT stabilizers in neurodegeneration is not straightforward. The main hypothesis focuses on the consequences of drug interactions on the MT lattice structure, which involve an axial expansion (2 Å per tubulin dimer) and a higher angle between lateral neighbors due to the formation of filaments with smaller diameter.[25,27] Similarly, we have found that LAU and PLA also modify the MT surface due to a direct effect on the angle between PFs, contributing to the formation of larger (LAU) or smaller (PLA) MTs, which very likely also modify the

recognition surface for cellular MAPs. Otherwise, we have identified PLA analogs able to stabilize MTs without inducing alterations on the MT lattice. In fact, the combination of MT stabilization without alterations of the filament structure with the low cytotoxicity of these compounds suggests that PLA analogs could be promising candidates for other clinical applications beyond cancer treatment. In conclusion, the work presented here highlights a mechanism for MT stabilization that contrasts with that known for taxane site binders. This fact allows the differential pharmacological modulation of MT shape and conformation depending on the MSA site targeted, which can contribute to scouting for new clinical applications by exploiting the LP site.

## STAR★METHODS

Detailed methods are provided in the online version of this paper and include the following:

- KEY RESOURCES TABLE
- RESOURCE AVAILABILITY
  - Lead contact
  - Materials availability
  - Data and code availability
- EXPERIMENTAL MODEL AND SUBJECT DETAILS
- METHOD DETAILS
  - Proteins and chemicals
  - Microtubule shear-flow alignment and X-ray fiber diffraction experiments
  - Molecular modelling
  - Biochemistry
  - Cell biology
  - Crystallization and crystal structure determination
- QUANTIFICATION AND STATISTICAL ANALYSIS

### SUPPLEMENTAL INFORMATION

Supplemental information can be found online at https://doi.org/10.1016/j.str.2022.11.006.

### AUTHOR CONTRIBUTIONS

Conceptualization, M.A.O. and J.F.D. Investigation, J.E-G., B.A-B., B.P., D.L-A., F.B., K.B., J.C., J.F., G-A., C.W., S.K., O.R., and D.M. Formal analysis, F.G., A.E.P., and M.A.O. Methodology, S.K. Writing – original draft, M.A.O., J.F.D., and J.E-G. Writing – review & editing, M.A.O., J.F.D., P.N., K-H.A., I.P., J.V.E., and F.G. Funding acquisition, M.A.O., J.F.D., A.E.P., and M.O.S. Resources, K-H.A., I.P., J.V.E., P.N., and J.C.M. Supervision, M.A.O., J.F.D., A.E.P., K-H.A., I.P., J.V.E., and P.N.

### REFERENCES

1. Borisy, G.G., and Taylor, E.W. (1967). The mechanism of action of colchicine. Binding of colchincine-^{3}H to cellular protein. J. Cell Biol. *34*, 535–548. https://doi.org/10.1083/jcb.34.2.535.

2. Ravelli, R.B.G., Gigant, B., Curmi, P.A., Jourdain, I., Lachkar, S., Sobel, A., and Knossow, M. (2004). Insight into tubulin regulation from a complex with colchicine and a stathmin-like domain. Nature *428*, 198–202. https://doi.org/10.1038/nature02393.

3. Wani, M.C., Taylor, H.L., Wall, M.E., Coggon, P., and McPhail, A.T. (1971). Plant antitumor agents. VI. The isolation and structure of taxol, a novel antileukemic and antitumor agent from Taxus brevifolia. J. Am. Chem. Soc. *93*, 2325–2327. https://doi.org/10.1091/mbc.E14-04-0916.

4. Nogales, E., Wolf, S.G., Khan, I.A., Ludueña, R.F., and Downing, K.H. (1995). Structure of tubulin at 6.5 Å and location of the taxol-binding site. Nature *375*, 424–427. https://doi.org/10.1038/375424a0.

5. Wilson, L., Creswell, K.M., and Chin, D. (1975). Mechanism of action of vinblastine. Binding of [acetyl-^{3}H]-vinblastine to embryonic chick brain tubulin and tubulin from sea urchin sperm tail outer doublet microtubules. Biochemistry *14*, 5586–5592. https://doi.org/10.1021/bi00697a008.

6. Gigant, B., Wang, C., Ravelli, R.B.G., Roussi, F., Steinmetz, M.O., Curmi, P.A., Sobel, A., and Knossow, M. (2005). Structural basis for the regulation of tubulin by vinblastine. Nature *435*, 519–522. https://doi.org/10.1038/nature03566.

7. Pryor, D.E., O'Brate, A., Bilcer, G., Díaz, J.F., Wang, Y., Wang, Y., Kabaki, M., Jung, M.K., Andreu, J.M., Ghosh, A.K., et al. (2002). The microtubule stabilizing agent laulimalide does not bind in the taxoid site, kills cells resistant to paclitaxel and epothilones, and may not require its epoxide moiety for activity. Biochemistry *41*, 9109–9115. https://doi.org/10.1021/bi020211b.

8. Gaitanos, T.N., Buey, R.M., Díaz, J.F., Northcote, P.T., Teesdale-Spittle, P., Andreu, J.M., and Miller, J.H. (2004). Peloruside A does not bind to the taxoid site on beta-tubulin and retains its activity in multidrug-resistant cell lines. Cancer Res. *64*, 5063–5067. https://doi.org/10.1158/0008-5472.CAN-04-0771.

9. Prota, A.E., Bargsten, K., Northcote, P.T., Marsh, M., Altmann, K.H., Miller, J.H., Díaz, J.F., and Steinmetz, M.O. (2014). Structural basis of microtubule stabilization by laulimalide and peloruside A. Angew. Chem. Int. Ed. Engl. *53*, 1621–1625. https://doi.org/10.1002/anie.201307749.

10. Usui, T., Watanabe, H., Nakayama, H., Tada, Y., Kanoh, N., Kondoh, M., Asao, T., Takio, K., Watanabe, H., Nishikawa, K., et al. (2004). The anticancer natural product pironetin selectively targets Lys352 of alpha-tubulin. Chem. Biol. *11*, 799–806. https://doi.org/10.1016/j.chembiol.2004.03.028.

11. Prota, A.E., Setter, J., Waight, A.B., Bargsten, K., Murga, J., Díaz, J.F., et al. (2016). Pironetin binds covalently to alphaCys316 and perturbs a

major loop and helix of alpha-tubulin to inhibit microtubule formation. J. Mol. Biol. *428*, 2981–2988. https://doi.org/10.1016/j.jmb.2016.06.023.

12. Yang, J., Wang, Y., Wang, T., Jiang, J., Botting, C.H., Liu, H., et al. (2016). Pironetin reacts covalently with cysteine-316 of α-tubulin to destabilize microtubule. Nat. Commun. *7*, 12103. https://doi.org/10.1038/ncomms12103.

13. Kupchan, S.M., Komoda, Y., Court, W.A., Thomas, G.J., Smith, R.M., Karim, A., Gilmore, C.J., Haltiwanger, R.C., and Bryan, R.F. (1972). Maytansine, a novel antileukemic ansa macrolide from Maytenus ovatus. J. Am. Chem. Soc. *94*, 1354–1356. https://doi.org/10.1021/ja00759a054.

14. Pera, B., Barasoain, I., Pantazopoulou, A., Canales, A., Matesanz, R., Rodriguez-Salarichs, J., García-Fernandez, L.F., Moneo, V., Jiménez-Barbero, J., Galmarini, C.M., et al. (2013). New interfacial microtubule inhibitors of marine origin, PM050489/PM060184, with potent antitumor activity and a distinct mechanism. ACS Chem. Biol. *8*, 2084–2094. https://doi.org/10.1021/cb400461j.

15. Prota, A.E., Bargsten, K., Díaz, J.F., Marsh, M., Cuevas, C., Liniger, M., et al. (2014). A new tubulin-binding site and pharmacophore for microtubule-destabilizing anticancer drugs. Proc. Natl. Acad. Sci. USA *111*, 13817–13821. https://doi.org/10.1073/pnas.1408124111.

16. Matthew, S., Chen, Q.-Y., Ratnayake, R., Fermaintt, C.S., Lucena-Agell, D., Bonato, F., Prota, A.E., Lim, S.T., Wang, X., Díaz, J.F., et al. (2021). Gatorbulin-1, a distinct cyclodepsipeptide chemotype, targets a seventh tubulin pharmacological site. Proc. Natl. Acad. Sci. USA *118*. e2021847118. https://doi.org/10.1073/pnas.2021847118.

17. Steinmetz, M.O., and Prota, A.E. (2018). Microtubule-targeting agents: strategies to hijack the cytoskeleton. Trends Cell Biol. *28*, 776–792. https://doi.org/10.1016/j.tcb.2018.05.001.

18. Jordan, M.A., and Wilson, L. (2004). Microtubules as a target for anticancer drugs. Nat. Rev. Cancer *4*, 253–265. https://doi.org/10.1038/nrc1317.

19. Weaver, B.A. (2014). How Taxol/paclitaxel kills cancer cells. Mol. Biol. Cell *25*, 2677–2681. https://doi.org/10.1091/mbc.E14-04-0916.

20. Fletcher, J.I., Williams, R.T., Henderson, M.J., Norris, M.D., and Haber, M. (2016). ABC transporters as mediators of drug resistance and contributors to cancer cell biology. Drug Resist. Updat. *26*, 1–9. https://doi.org/10.1016/j.drup.2016.03.001.

21. Kavallaris, M., Kuo, D.Y., Burkhart, C.A., Regl, D.L., Norris, M.D., Haber, M., and Horwitz, S.B. (1997). Taxol-resistant epithelial ovarian tumors are associated with altered expression of specific beta-tubulin isotypes. J. Clin. Invest. *100*, 1282–1293. https://doi.org/10.1172/JCI119642.

22. Kavallaris, M. (2010). Microtubules and resistance to tubulin-binding agents. Nat. Rev. Cancer *10*, 194–204. https://doi.org/10.1038/nrc2803.

23. Park, S.B., Lin, C.S.Y., Krishnan, A.V., Friedlander, M.L., Lewis, C.R., and Kiernan, M.C. (2011). Early, progressive, and sustained dysfunction of sensory axons underlies paclitaxel-induced neuropathy. Muscle Nerve *43*, 367–374. https://doi.org/10.1002/mus.21874.

24. Franker, M.A.M., and Hoogenraad, C.C. (2013). Microtubule-based transport - basic mechanisms, traffic rules and role in neurological pathogenesis. J. Cell Sci. *126*, 2319–2329. https://doi.org/10.1242/jcs.115030.

25. Estévez-Gallego, J., Josa-Prado, F., Ku, S., Buey, R.M., Balaguer, F.A., Prota, A.E., Lucena-Agell, D., Kamma-Lorger, C., Yagi, T., Iwamoto, H., et al. (2020). Structural model for differential cap maturation at growing microtubule ends. Elife *9*, e50155. https://doi.org/10.7554/eLife.50155.

26. Prota, A.E., Bargsten, K., Zurwerra, D., Field, J.J., Díaz, J.F., Altmann, K.H., and Steinmetz, M.O. (2013). Molecular mechanism of action of microtubule-stabilizing anticancer agents. Science *339*, 587–590. https://doi.org/10.1126/science.1230582.

27. Kellogg, E.H., Hejab, N.M.A., Howes, S., Northcote, P., Miller, J.H., Díaz, J.F., Downing, K.H., and Nogales, E. (2017). Insights into the distinct mechanisms of action of taxane and non-taxane microtubule stabilizers from cryo-EM structures. J. Mol. Biol. *429*, 633–646. https://doi.org/10.1016/j.jmb.2017.01.001.

28. Manka, S.W., and Moores, C.A. (2018). The role of tubulin-tubulin lattice contacts in the mechanism of microtubule dynamic instability. Nat. Struct. Mol. Biol. *25*, 607–615. https://doi.org/10.1038/s41594-018-0087-8.

29. Gornstein, E., and Schwarz, T.L. (2014). The paradox of paclitaxel neurotoxicity: mechanisms and unanswered questions. Neuropharmacology *76*, 175–183. https://doi.org/10.1016/j.neuropharm.2013.08.016.

30. Mooberry, S.L., Tien, G., Hernandez, A.H., Plubrukarn, A., and Davidson, B.S. (1999). Laulimalide and isolaulimalide, new paclitaxel-like microtubule-stabilizing agents. Cancer Res. *59*, 653–660.

31. Liu, J., Towle, M.J., Cheng, H., Saxton, P., Reardon, C., Wu, J., Murphy, E.A., Kuznetsov, G., Johannes, C.W., Tremblay, M.R., et al. (2007). In vitro and in vivo anticancer activities of synthetic (-)-laulimalide, a marine natural product microtubule stabilizing agent. Anticancer Res. *27*, 1509–1518.

32. West, L.M., Northcote, P.T., and Battershill, C.N. (2000). Peloruside A: a potent cytotoxic macrolide isolated from the New Zealand marine sponge Mycale sp. J. Org. Chem. *65*, 445–449. https://doi.org/10.1021/jo991296y.

33. Pera, B., Razzak, M., Trigili, C., Pineda, O., Canales, A., Buey, R.M., Jiménez-Barbero, J., Northcote, P.T., Paterson, I., Barasoain, I., and Díaz, J.F. (2010). Molecular recognition of peloruside A by microtubules. The C24 primary alcohol is essential for biological activity. Chembiochem *11*, 1669–1678. https://doi.org/10.1002/cbic.201000294.

34. Meyer, C.J., Krauth, M., Wick, M.J., Shay, J.W., Gellert, G., De Brabander, J.K., Northcote, P.T., and Miller, J.H. (2015). Peloruside A inhibits growth of human lung and breast tumor xenografts in an athymic *nu/nu* mouse model. Mol. Cancer Ther. *14*, 1816–1823. https://doi.org/10.1158/1535-7163.Mct-15-0167.

35. Kanakkanthara, A., Northcote, P.T., and Miller, J.H. (2016). Peloruside A: a lead non-taxoid-site microtubule-stabilizing agent with potential activity against cancer, neurodegeneration, and autoimmune disease. Nat. Prod. Rep. *33*, 549–561. https://doi.org/10.1039/c5np00146c.

36. Das, V., and Miller, J.H. (2012). Non-taxoid site microtubule-stabilizing drugs work independently of tau overexpression in mouse N2a neuroblastoma cells. Brain Res. *1489*, 121–132. https://doi.org/10.1016/j.brainres.2012.10.022.

37. Liao, X., Wu, Y., and De Brabander, J.K. (2003). Total synthesis and absolute configuration of the novel microtubule-stabilizing agent peloruside A. Angew. Chem. Int. Ed. Engl. *42*, 1648–1652. https://doi.org/10.1002/anie.200351145.

38. Jin, M., and Taylor, R.E. (2005). Total synthesis of (+)-Peloruside A. Org. Lett. *7*, 1303–1305. https://doi.org/10.1021/ol050070g.

39. McGowan, M.A., Stevenson, C.P., Schiffler, M.A., and Jacobsen, E.N. (2010). An enantioselective total synthesis of (+)-Peloruside A. Angew. Chem. Int. Ed. Engl. *49*, 6147–6150. https://doi.org/10.1002/anie.201002177.

40. Hoye, T.R., Jeon, J., Kopel, L.C., Ryba, T.D., Tennakoon, M.A., and Wang, Y. (2010). Total synthesis of peloruside A through kinetic lactonization and relay ring-closing metathesis cyclization reactions. Angew. Chem. Int. Ed. Engl. *49*, 6151–6155. https://doi.org/10.1002/anie.201002293.

41. Alushin, G.M., Lander, G.C., Kellogg, E.H., Zhang, R., Baker, D., and Nogales, E. (2014). High-resolution microtubule structures reveal the structural transitions in αβ-tubulin upon GTP hydrolysis. Cell *157*, 1117–1129. https://doi.org/10.1016/j.cell.2014.03.053.

42. Sánchez-Murcia, P.A., Mills, A., Cortés-Cabrera, Á., and Gago, F. (2019). Unravelling the covalent binding of zampanolide and taccalonolide AJ to a minimalist representation of a human microtubule. J. Comput. Aided Mol. Des. *33*, 627–644. https://doi.org/10.1007/s10822-019-00208-w.

43. Fedorov, V.A., Orekhov, P.S., Kholina, E.G., Zhmurov, A.A., Ataullakhanov, F.I., Kovalenko, I.B., and Gudimchuk, N.B. (2019). Mechanical properties of tubulin intra- and inter-dimer interfaces and their implications for microtubule dynamic instability. PLoS Comput. Biol. *15*, e1007327. https://doi.org/10.1371/journal.pcbi.1007327.

44. Havelka, D., Deriu, M.A., Cifra, M., and Kučera, O. (2017). Deformation pattern in vibrating microtubule: structural mechanics study based on an atomistic approach. Sci. Rep. *7*, 4227. https://doi.org/10.1038/s41598-017-04272-w.

45. Kyte, J. (2003). The basis of the hydrophobic effect. Biophys. Chem. *100*, 193–203. https://doi.org/10.1016/s0301-4622(02)00281-8.

46. Martin, S.F., and Clements, J.H. (2013). Correlating structure and energetics in protein-ligand interactions: paradigms and paradoxes. Annu. Rev. Biochem. *82*, 267–293. https://doi.org/10.1146/annurev-biochem-060410-105819.

47. Díaz, J.F., Strobe, R., Engelborghs, Y., Souto, A.A., and Andreu, J.M. (2000). Molecular recognition of taxol by microtubules. Kinetics and thermodynamics of binding of fluorescent taxol derivatives to an exposed site. J. Biol. Chem. *275*, 26265–26276. https://doi.org/10.1074/jbc.M003120200.

48. Díaz, J.F., Barasoain, I., and Andreu, J.M. (2003). Fast kinetics of Taxol binding to microtubules. Effects of solution variables and microtubule-associated proteins. J. Biol. Chem. *278*, 8407–8419. https://doi.org/10.1074/jbc.M211163200.

49. Buey, R.M., Díaz, J.F., Andreu, J.M., O'Brate, A., Giannakakou, P., Nicolaou, K.C., Sasmal, P.K., Ritzén, A., and Namoto, K. (2004). Interaction of epothilone analogs with the paclitaxel binding site; relationship between binding affinity, microtubule stabilization, and cytotoxicity. Chem. Biol. *11*, 225–236. https://doi.org/10.1016/j.chembiol.2004.01.014.

50. Buey, R.M., Barasoain, I., Jackson, E., Meyer, A., Giannakakou, P., Paterson, I., Mooberry, S., Andreu, J.M., and Díaz, J.F. (2005). Microtubule interactions with chemically diverse stabilizing agents: thermodynamics of binding to the paclitaxel site predicts cytotoxicity. Chem. Biol. *12*, 1269–1279. https://doi.org/10.1016/j.chembiol.2005.09.010.

51. Matesanz, R., Barasoain, I., Yang, C.G., Wang, L., Li, X., de Inés, C., Coderch, C., Gago, F., Barbero, J.J., Andreu, J.M., et al. (2008). Optimization of taxane binding to microtubules. Binding affinity decomposition and incremental construction of a high-affinity analogue of paclitaxel. Chem. Biol. *15*, 573–585. https://doi.org/10.1016/j.chembiol.2008.05.008.

52. Trigili, C., Barasoain, I., Sánchez-Murcia, P.A., Bargsten, K., Redondo-Horcajo, M., Nogales, A., Gardner, N.M., Meyer, A., Naylor, G.J., Gómez-Rubio, E., et al. (2016). Structural determinants of the dictyostatin chemotype for tubulin binding affinity and antitumor activity against taxane- and epothilone-resistant cancer cells. ACS Omega *1*, 1192–1204. https://doi.org/10.1021/acsomega.6b00317.

53. Paterson, I., Menche, D., Håkansson, A.E., Longstaff, A., Wong, D., Barasoain, I., Buey, R.M., and Díaz, J.F. (2005). Design, synthesis and biological evaluation of novel, simplified analogues of laulimalide: modification of the side chain. Bioorg. Med. Chem. Lett. *15*, 2243–2247. https://doi.org/10.1016/j.bmcl.2005.03.018.

54. Wullschleger, C.W., Gertsch, J., and Altmann, K.-H. (2013). Synthesis and biological activity of 7, 8, 9-trideoxy- and 7R DesTHP-peloruside A. Chemistry *19*, 13105–13111. https://doi.org/10.1002/chem.201301796.

55. Prota, A.E., Magiera, M.M., Kuijpers, M., Bargsten, K., Frey, D., Wieser, M., Jaussi, R., Hoogenraad, C.C., Kammerer, R.A., Janke, C., and Steinmetz, M.O. (2013). Structural basis of tubulin tyrosination by tubulin tyrosine ligase. J. Cell Biol. *200*, 259–270. https://doi.org/10.1083/jcb.201211017.

56. Kollman, J.M., Merdes, A., Mourey, L., and Agard, D.A. (2011). Microtubule nucleation by γ-tubulin complexes. Nat. Rev. Mol. Cell Biol. *12*, 709–721. https://doi.org/10.1038/nrm3209.

57. Akhmanova, A., and Steinmetz, M.O. (2010). Microtubule +TIPs at a glance. J. Cell Sci. *123*, 3415–3419. https://doi.org/10.1242/jcs.062414.

58. Akhmanova, A., and Steinmetz, M.O. (2019). Microtubule minus-end regulation at a glance. J. Cell Sci. *132*, jcs227850. https://doi.org/10.1242/jcs.227850.

59. Janke, C., and Magiera, M.M. (2020). The tubulin code and its role in controlling microtubule properties and functions. Nat. Rev. Mol. Cell Biol. *21*, 307–326. https://doi.org/10.1038/s41580-020-0214-3.

60. Ludueña, R.F., and Banerjee, A. (2008). The isotypes of tubulin. In The Role of Microtubules in Cell Biology, Neurobiology, and Oncology, T. Fojo, ed. (Humana Press), pp. 123–175. https://doi.org/10.1007/978-1-59745-336-3_6.

61. Petry, S. (2016). Mechanisms of mitotic spindle assembly. Annu. Rev. Biochem. *85*, 659–683. https://doi.org/10.1146/annurev-biochem-060815-014528.

62. Debs, G.E., Cha, M., Liu, X., Huehn, A.R., and Sindelar, C.V. (2020). Dynamic and asymmetric fluctuations in the microtubule wall captured by high-resolution cryoelectron microscopy. Proc. Natl. Acad. Sci. USA *117*, 16976–16984. https://doi.org/10.1073/pnas.2001546117.

63. Schöll, M., Lockhart, S.N., Schonhaut, D.R., O'Neil, J.P., Janabi, M., Ossenkoppele, R., Baker, S.L., Vogel, J.W., Faria, J., Schwimmer, H.D., et al. (2016). PET imaging of tau deposition in the aging human brain. Neuron *89*, 971–982. https://doi.org/10.1016/j.neuron.2016.01.028.

64. Ballatore, C., Brunden, K.R., Huryn, D.M., Trojanowski, J.Q., Lee, V.M.Y., and Smith, A.B., 3rd. (2012). Microtubule stabilizing agents as potential treatment for Alzheimer's disease and related neurodegenerative tauopathies. J. Med. Chem. *55*, 8979–8996. https://doi.org/10.1021/jm301079z.

65. Brunden, K.R., Lee, V.M.Y., Smith, A.B., Trojanowski, J.Q., and Ballatore, C. (2017). Altered microtubule dynamics in neurodegenerative disease: therapeutic potential of microtubule-stabilizing drugs. Neurobiol. Dis. *105*, 328–335. https://doi.org/10.1016/j.nbd.2016.12.021.

66. Yang, C.G., Barasoain, I., Li, X., Matesanz, R., Liu, R., Sharom, F.J., Yin, D.L., Díaz, J.F., and Fang, W.S. (2007). Overcoming tumor drug resistance with high-affinity taxanes: a SAR study of C2-modified 7-acyl-10-deacetyl cephalomannines. ChemMedChem *2*, 691–701. https://doi.org/10.1002/cmdc.200700002.

67. Díaz, J.F., Menéndez, M., and Andreu, J.M. (1993). Thermodynamics of ligand-induced assembly of tubulin. Biochemistry *32*, 10067–10077. https://doi.org/10.1021/bi00089a023.

68. Paterson, I., Bergmann, H., Menche, D., and Berkessel, A. (2004). Synthesis of novel 11-desmethyl analogues of laulimalide by Nozaki-Kishi coupling. Org. Lett. *6*, 1293–1295. https://doi.org/10.1021/ol049791q.

69. Sugiyama, T., Miyashiro, D., Takao, D., Iwamoto, H., Sugimoto, Y., Wakabayashi, K., and Kamimura, S. (2009). Quick shear-flow alignment of biological filaments for X-ray fiber diffraction facilitated by methylcellulose. Biophys,. J. *97*, 3132–3138. https://doi.org/10.1016/j.bpj.2009.09.041.

70. Kamimura, S., Fujita, Y., Wada, Y., Yagi, T., and Iwamoto, H. (2016). X-ray fiber diffraction analysis shows dynamic changes in axial tubulin repeats in native microtubules depending on paclitaxel content, temperature and GTP-hydrolysis. Cytoskeleton *73*, 131–144. https://doi.org/10.1002/cm.21283.

71. Ma, Y.-T., Yang, Y., Cai, P., Sun, D.-Y., Sánchez-Murcia, P.A., Zhang, X.-Y., Jia, W.-Q., Lei, L., Guo, M., Gago, F., et al. (2018). A series of enthalpically optimized docetaxel analogues exhibiting enhanced antitumor activity and water solubility. J. Nat. Prod. *81*, 524–533. https://doi.org/10.1021/acs.jnatprod.7b00857.

72. Anandakrishnan, R., Aguilar, B., and Onufriev, A.V. (2012). H++ 3.0: automating pK prediction and the preparation of biomolecular structures for atomistic molecular modeling and simulations. Nucleic Acids Res. *40*, W537–W541. https://doi.org/10.1093/nar/gks375.

73. Löwe, J., Li, H., Downing, K.H., and Nogales, E. (2001). Refined structure of α,β-tubulin at 3.5 Å resolution. J. Mol. Biol. *313*, 1045–1057. https://doi.org/10.1006/jmbi.2001.5077.

74. Salomon-Ferrer, R., Götz, A.W., Poole, D., Le Grand, S., and Walker, R.C. (2013). Routine microsecond molecular dynamics simulations with AMBER on GPUs. 2. Explicit solvent particle mesh Ewald. J. Chem. Theory Comput. *9*, 3878–3888. https://doi.org/10.1021/ct400314y.

75. Ryckaert, J.-P., Ciccotti, G., and Berendsen, H.J. (1977). Numerical integration of the cartesian equations of motion of a system with constraints: molecular dynamics of n-alkanes. J. Comput. Phys. 23, 327–341. https://doi.org/10.1016/0021-9991(77)90098-5.

76. Le Grand, S., Götz, A.W., and Walker, R.C. (2013). SPFP: speed without compromise—a mixed precision model for GPU accelerated molecular dynamics simulations. Comput. Phys. Commun. 184, 374–380. https://doi.org/10.1016/j.cpc.2012.09.022.

77. Roe, D.R., and Cheatham, T.E. (2013). PTRAJ and CPPTRAJ: software for processing and analysis of molecular dynamics trajectory data. J. Chem. Theory Comput. 9, 3084–3095. https://doi.org/10.1021/ct400341p.

78. Klett, J., Núñez-Salgado, A., Dos Santos, H.G., Cortés-Cabrera, Á., Perona, A., Gil-Redondo, R., Abia, D., Gago, F., and Morreale, A. (2012). MM-ISMSA: an ultrafast and accurate scoring function for protein–protein docking. J. Chem. Theory Comput. 8, 3395–3408. https://doi.org/10.1021/ct300497z.

79. Díaz, J.F., and Andreu, J.M. (1993). Assembly of purified GDP-tubulin into microtubules induced by taxol and taxotere: reversibility, ligand stoichiometry, and competition. Biochemistry 32, 2747–2755. https://doi.org/10.1021/bi00062a003.

80. de Ines, C., Leynadier, D., Barasoain, I., Peyrot, V., Garcia, P., Briand, C., Rener, G.A., and Temple, C., Jr. (1994). Inhibition of microtubules and cell cycle arrest by a new 1-deaza-7, 8-dihydropteridine antitumor drug, CI 980, and by its chiral isomer, NSC 613863. Cancer Res. 54, 75–84.

81. Kabsch, W. (2010). Xds. Acta Crystallogr. D Biol. Crystallogr. 66, 125–132. https://doi.org/10.1107/S0907444909047337.

82. Winn, M.D., Ballard, C.C., Cowtan, K.D., Dodson, E.J., Emsley, P., Evans, P.R., Keegan, R.M., Krissinel, E.B., Leslie, A.G.W., McCoy, A., et al. (2011). Overview of the CCP4 suite and current developments. Acta Crystallogr. D Biol. Crystallogr. 67, 235–242. https://doi.org/10.1107/S0907444910045749.

83. Adams, P.D., Afonine, P.V., Bunkóczi, G., Chen, V.B., Davis, I.W., Echols, N., Headd, J.J., Hung, L.-W., Kapral, G.J., Grosse-Kunstleve, R.W., et al. (2010). PHENIX: a comprehensive python-based system for macromolecular structure solution. Acta Crystallogr. D Biol. Crystallogr. 66, 213–221. https://doi.org/10.1107/S0907444909052925.

84. McCoy, A.J., Grosse-Kunstleve, R.W., Adams, P.D., Winn, M.D., Storoni, L.C., and Read, R.J. (2007). Phaser crystallographic software. J. Appl. Crystallogr. 40, 658–674. https://doi.org/10.1107/S0021889807021206.

85. Emsley, P., Lohkamp, B., Scott, W.G., and Cowtan, K. (2010). Features and development of coot. Acta Crystallogr. D Biol. Crystallogr. 66, 486–501. https://doi.org/10.1107/S0907444910007493.

## STAR★METHODS

### KEY RESOURCES TABLE

| REAGENT or RESOURCE | SOURCE | IDENTIFIER |
|---|---|---|
| **Antibodies** | | |
| DM1A | Sigma-Aldrich | T6199; RRID: AB_477583 |
| **Bacterial and virus strains** | | |
| *E. coli* BL21 DE3 | Novagen | N19893 |
| **Chemicals, peptides, and recombinant proteins** | | |
| Guanosine-5'-[($\alpha$,$\beta$)-methyleno] triphosphate (GMPCPP) | Jena Bioscience | NU-405L |
| Paclitaxel | NCI, USA | PTX |
| Peloruside | WU, ZN | PLA |
| Laulimalide | Paterson et al.[53] | LAU |
| IP01 | Paterson et al.[53] | N/A |
| IP02 | Paterson et al.[53] | N/A |
| IP03 | Paterson et al.[53] | N/A |
| IP05 | Paterson et al.[53] | N/A |
| IP06 | Paterson et al.[53] | N/A |
| IP07 | Paterson et al.[53] | N/A |
| IP08 | Paterson et al.[53] | N/A |
| IP09 | Paterson et al.[53] | N/A |
| IP10 | Paterson et al.[53] | N/A |
| CW329 | Wullschleger et al.[54] | N/A |
| CW190.2 | Wullschleger et al.[54] | N/A |
| CW235 | Wullschleger et al.[54] | N/A |
| Pelophen B | U Ghent, Belgium | PPH |
| Flutax-2 | IMM, China | FTX2 |
| **Deposited data** | | |
| T2R-TTL-CW190 complex | This paper | PDB: 8A01 |
| T2R-TTL-PPH complex | This paper | PDB: 7ZX2 |
| T2R-TTL-Colchicine complex | PDB<br>PDB https://doi.org/10.2210/pdb4O2B/pdb | PDB: 4O2B |
| CryoEM reconstruction of peloruside-stabilized microtubule | PDB<br>PDB https://doi.org/10.2210/pdb5SYC/pdb | PDB: 5SYC |
| T2R-TTL-Laulimalide complex | Protein Data Bank<br>PDB https://doi.org/10.2210/pdb4O4H/pdb | PDB: 4O4H |
| T2R-TTL-Peloruside A complex | Protein Data Bank<br>PDB https://doi.org/10.2210/pdb4O4J/pdb | PDB: 4O4J |
| T24-TTL-Discodermolide complex | Protein Data Bank<br>PDB https://doi.org/10.2210/pdb5LXT/pdb | PDB: 5LXT |
| **Experimental models: Cell lines** | | |
| Human A549 non-small cell lung carcinoma cells | ATTC | CCL-185 |
| Human ovarian carcinomas A2780 | ECACC | 93112519 |
| Human ovarian carcinomas A2780AD | ECACC | 93112519 |
| **Recombinant DNA** | | |
| ggTTL (in NSKN1) | Prota et al.[55] | N/A |
| RB3 (in pET3d) | Ravelli et al.[2] | N/A |

*(Continued on next page)*

*Continued*

| REAGENT or RESOURCE | SOURCE | IDENTIFIER |
|---|---|---|
| Software and algorithms | | |
| XDS | Kabsch[81] | https://xds.mr.mpg.de/ |
| AIMLESS | Winn et al.[82] | https://www.ccp4.ac.uk/html/aimless.html |
| PHASER | McCoy et al.[84] | https://www.phaser.cimr.cam.ac.uk/index.php/Phaser_Crystallographic_Software |
| PHENIX | Adams et al.[83] | https://phenix-online.org/download/ |
| COOT | Emsley et al.[85] | https://www2.mrc-lmb.cam.ac.uk/personal/pemsley/coot/ |
| ImageJ 1.58j8 | Wayne Rasband, Bethesda, USA | https://imagej.nih.gov/ij |
| XRTools | ESRF, Grenoble | N/A |
| H++ 3.0 Web server | Anandakrishnan et al.[72] | http://newbiophysics.cs.vt.edu/H++/ |
| SHAKE algorithm | Ryckaert et al.[75] | N/A |
| AMBER 16 | Salomon-Ferrer et al.[74] | https://ambermd.org/ |
| MM-ISMSA | Klett et al.[78] | https://github.com/accsc/cMMISMSA |
| SigmaPlot 14.5 | Systat Software | https://www.addlink.es/productos/sigmaplot |

## RESOURCE AVAILABILITY

### Lead contact
Further information and request for resources and reagents should be directed to and will be fulfilled by the lead contact, María A. Oliva (marian@cib.csic.es).

### Materials availability
This study did not generate unique reagents.

There are restrictions to the availability of Pelophen B (PPB) due to patent PCT/EP2014/075903.

### Data and code availability
The structure of T2R-TTL-CW190 and T2R-TTL-PPH have been deposited at PDB and are publicly available as of the date of publication. Accession numbers are listed in the key resources table. This paper analyzes existing, publicly available data. These accession numbers for the datasets are listed in the key resources table. All reported data in this paper will be shared by the lead contact upon request.

This paper does not report original code.

Any additional information required to reanalyze the data reported in this paper is available from the lead contact upon request.

## EXPERIMENTAL MODEL AND SUBJECT DETAILS

Human A549 non-small cell lung carcinoma cells, as well as human ovarian carcinomas A2780 and its P-glycoprotein overexpressing counterpart A2780AD were cultured at 37°C in DMEM supplemented with 10% fetal calf serum, 2 mM L-glutamine, 1 mM pyruvate, 40 µg/mL gentamycin, 100 IU/mL penicillin and 100 µg/mL streptomycin in a 5% $CO_2$ air atmosphere. Antiproliferation assays were performed as described.[66] In brief, the cytotoxicity of the compounds was evaluated by means of MTT assays, where $10^4$-$10^5$ cells, depending on the assessed cell line, were grown for 24 h in 96-well plates. Then, increasing concentrations of the targeted compound was added and left them incubate for additional 24 h. Subsequently, the MTT reaction was performed for 2 h and stopped using a solution of DMF-SDS. Finally, plates were analyzed in an Appliskan (Thermo Scientific) plate reader at 570 and 690 nm IC50 values were obtained by fitting the experimental data to a four-parameter logistic curve using SigmaPlot 14.5 software package (Systat Software, Inc., San Jose, CA, USA). *Escherichia coli* BL21 (DE3) were cultured in LB medium supplemented with 100 µg/mL ampicillin (RB3 expression) or 50 µg/mL kanamycin (TTL expression). Cells were grown up to an optical density of 0.8 and the expression of these proteins were induced by the addition of 1 mM Isopropyl β-D-1-thiogalactopyranoside (IPTG) for 4 h at 37°C or 20 hours at 20°C, respectively.

## METHOD DETAILS

### Proteins and chemicals
Purified calf brain tubulin and chemicals were obtained as previously described.[67] In brief, 6–8 freshly slaughtered calf brains were chopped and liquefied in PMS buffer (10 mM NaPi, 0.5 mM $MgCl_2$, 0.24 M sucrose pH 7.0). The homogenize was clarified by

centrifugation at 20,500 g for 40 min and the clarified solution was fractioned in a two-step ammonium sulfate precipitation: 32% saturation in a first step, discarding the pelleted proteins and up to 43% saturation in the second, in which tubulin is part of the pelleted protein. The pellet was then resuspended in PMG buffer (10 mM NaPi, 0.5 mM MgCl₂, 0.1 mM GTP pH 7.0) and treated with 15 mL of DEAE-Sephadex A50 resin to perform a batch anion exchange chromatography. Two elution steps were used: 0.4M KCl PMG to remove contaminants and 0.8M KCl to elute tubulin. The resulting tubulin solution was concentrated by precipitation with 43% ammonium sulfate and centrifugation at 30,000 g for 60 min, 4°C. The pelleted protein was then dissolved in PMG buffer and desalted using a 400 mL Sephadex G-25 column. Fractions were selected by its ability to aggregate in presence of 30 mM MgCl₂. These fractions were pooled and dialyzed for 16 h using Slyde-a-Lyzer dialysis cassettes with a MWCO of 10 kDa against PMG 0.25 M Trehalose. The final tubulin solution was aliquoted, snap frozen and preserved in liquid nitrogen upon use. The stathmin-like domain of RB3 and the chicken TTL protein preparations were done as described previously.[2,55] In brief, RB3 was expressed in *Escherichia coli* BL21 cells that were dissolved in 20 mM Tris, 1 mM EGTA, 2 mM DTT, pH 8.0 supplemented with protease inhibitors, and broken on a French press (Thermo Fischer) at 1200 psi. Lysates were clarified by centrifugation at 17,000 g, 4°C for 15 min. The supernatant was warmed at 95°C for 10 min and centrifuged at 15,000 g for 60 min. Then, it was loaded in a fast-flow Q-sepharose column (GE healthcare) for anionic exchange, in which RB3 was eluted using a 20 Column Volume gradient from 0 mM to 500 mM NaCl in the lysis buffer. Fractions containing RB3 were concentrated using Amicon MWCO 10 (Merck-Millipore) and loaded into a Superdex 75 column equilibrated with buffer 10 mM HEPES, 150 mM NaCl, 2 mM DTT, pH 7.2. Fractions containing pure RB3 were pooled, concentrated aliquoted, snap frozen in liquid nitrogen and storeaged at −80°C upon use. TTL protein was expressed in *Escherichia coli* BL21 cells that were dissolved in 50 mM Tris, 1 M NaCl, 10% Glycerol, 2.5 mM MgCl₂, pH 7.5 supplemented with protease inhibitors, PMSF and DNAse enzyme. Bacteria cells were broken on a French press (Thermo Fischer) at 1200 psi. Lysates were clarified by centrifugation at 100,000 g, 4°C for 45 min. The clarified lysate was then loaded in a 5 mL His-Trap affinity column (GE Healthcare) equilibrated in lysis buffer. After washing with 20 CV of 20 mM imidazole, TTL was eluted in 10 CV of 250 mM imidazole. Fractions containing TTL were pooled, concentrated using an Amicon MWCO 30 (Merck Millipore) and loaded on a Superdex 200 column equilibrated with 50 mM Bis-Tris Propane, 200 mM NaCl, 2.5 mM MgCl₂, 5 mM β-mercaptoethanol, 1% Glycerol, pH 6.5. Fractions containing a visual purity >90% were pooled and concentrated up to 20 mg/mL. Final TTL solution was snap-frozen in liquid nitrogen and stored at −80°C upon use. Crosslinked stabilized MTs (MTX) in which the LP site is preserved were prepared as described in.[48] In brief, 40–60 mg of pure tubulin were equilibrated in 10 mM NaPi, 3.4 M glycerol, 1 mM EGTA pH 7.0. The protein was clarified by centrifugation at 100,000 g, 4°C for 10 min and supplemented with 6 mM MgCl₂ and 1 mM GTP to induce MT polymerization at 37°C for 40 min. Then, MTs were cross-linked with 0.2% glutaraldehyde at 37°C for 10 min. Glutaraldehyde in excess after the cross-linking reaction was reduced by the addition of 40 mM NaBH₄, incubating the mixture at 4°C for 20 min. Final MT solution was dialyzed against the tubulin equilibration buffer, supplemented with 0.1 mM GTP and 6 mM MgCl₂. The resulting MT suspension was drop-snap frozen and stored in liquid nitrogen upon use. The concentration of sites in the preserved MTs was calculated using the stoichiometry of Flutax-2 binding.[47]

Synthesis and characterization of LAU, IP01, IP02, IP05, IP06, IP07, IP08, IP09, IP10 is described in.[53] Synthesis and characterization of IP03 is described in.[68] Synthesis and characterization of CW329, CW190.2, CW235 is described in.[54] Synthesis and characterization of Pelophen B is described in patent PCT/EP2014/075903. All compounds were diluted in 99.8% D6 DMSO (Merck) to a final concentration of 20 mM and stored at −20°C. All compounds are >95% pure by HPLC analysis.

### Microtubule shear-flow alignment and X-ray fiber diffraction experiments

X-ray fiber diffraction data were collected in beamline BL11-NDC-SWEET of ALBA Synchrotron. The energy of the incident photons was 15 KeV or equivalently a wavelength, λ, of 0.827 Å.[25] Purified bovine brain tubulin was diluted to a final concentration of 100 μM in PM buffer (0.1 M PIPES, 1 mM EGTA, 0.2 mM Tris, 1 mM DTT, 3 mM MgCl₂ pH 6.8) containing either 2 mM GTP or 0.5 mM GMPCPP. All samples were incubated for 20 min at 37°C to induce the maximum fraction of polymerized tubulin and then, were mixed in a 1:1 volume ratio with PM buffer 3 mM MgCl₂ containing 2% methylcellulose (MO512; Sigma-Aldrich). Samples were centrifuged 10 s at 2,000 g to eliminate air bubbles and transferred to the space between a quartz disc and a ring-shaped cover slip arranged in the shear-flow device.[69,70] The device was kept at 37°C during measurements and the quartz disc rotates at 10 r.p.s to achieve the shear flow alignment. The SAXS diffraction patterns were collected by means of a single photon counting detector, Dectris PILATUS3S-1M, with an active area of 168.7 × 179.4 mm², an effective pixel size of 172 × 172 μm² and a dynamic range of 20 bits. Several experiments were performed collecting 150 s exposure time images. Background images were acquired in the same conditions, using PM buffer containing 3 mM MgCl₂ with 1% methylcellulose without tubulin. A total 24 diffraction images were averaged for each condition and background subtracted using ImageJ (version 1.51j8; Wayne Rasband, National Institutes of Health, Bethesda, USA). Angular image integrations were performed using XRTools software (Obtained upon request from beamline BM26-DUBBLE of the European Synchrotron Radiation Facility (ESRF)), where the spatial calibration was obtained from Ag-Behenate powder diffraction. Radial structural parameters (MT diameter and average inter-PT distances) and dimer/monomer length (from the 4th harmonic of the first layer-line signals) were determined as described in.[25] In brief, for radial structural parameters we analyzed the central-equatorial intensity profile ($l = 0$), where the intensity of this layer line at a reciprocal distance result from a MT mixed population with different protofilament numbers. Considering the fraction of MTs with $n$ protofilaments, the resulting intensity was deconvolved as the sum of intensities of individual structure functions and Equation 6 in the reference was used for iterative fitting by least squares of the experimental intensities using the Solver function in Excel (Microsoft, 2010 version). For the determination of the average monomer lengths, we analyzed the intensity profile of the central-meridional signals. The 4th harmonic of the first layer-line ($l = 4$)) was fitted to a

single-peaked Lorentzian function using Sigma-Plot software (version 12.0), in which the position of the maximum of intensity corresponds to ¼ of the average monomer length at the reciprocal space. See also Figures S1 and S3 and Table S1.

## Molecular modelling

Our reduced representation of a bovine MT for simulation purposes consists of the $\alpha_1:\beta_1:\alpha_2$ subunits from one PF together with the closely interacting $\alpha_{1'}:\beta_{1'}:\alpha_{2'}$ subunits from a neighboring PF. The complexes containing either LAU or PLA were built essentially as described earlier for other tubulin:ligand complexes,[42,52,71] in this case using the cryo-EM reconstruction of a naked MT in complex with PLA (PDB: 5syc, 3.5 Å resolution). In brief, (i) the template $\alpha$- and $\beta$-subunits were selected from the biological assembly of PDB: 3syc representing the cryo-EM reconstruction of a naked MT in complex with PLA at 3.5 Å resolution; and (ii) missing residues 36–48 in the four $\alpha$ subunits were added and the two guanosine-diphosphate (GDP) and four guanosine-triphosphate (GTP) molecules in the nucleotide-binding sites were incorporated together with their coordinated $Mg^{2+}$ ions. The docked poses of LAU (PDB: 4o4h, 2.1 Å resolution) and PLA (PDB: 4o4j, 2.2 Å resolution) within the LP site in the $\alpha,\beta$-tubulin dimers solved by X-ray crystallography[9] were used to place LAU and PLA at the inter-PF site of $\beta$-tubulin. Addition of hydrogen atoms to each protein ensemble and computation of the protonation state of titratable groups at pH 6.8 were carried out using the H++ 3.0 Web server.[72] For consistency with the Protein Data Bank, residue numbering and secondary structure assignment in this article follow the $\alpha$-tubulin-based definitions given in.[73]

Optimal adaptation of the ligands to the binding site was achieved by performing a steepest-descent energy minimization and the complexes were then immersed in a cubic box of TIP3P waters. Electroneutrality was achieved by addition of $Na^+$ ions at electrostatically favored positions and, each system was simulated under periodic boundary conditions. Electrostatic interactions were computed using the particle mesh Ewald method[74] with a grid spacing of 1 Å. The SHAKE algorithm[75] was applied to all bonds involving hydrogens, the integration step was 2.0 fs, and the cutoff distance for the non-bonded interactions was 9 Å. The unrestrained molecular dynamics simulations were run for 250 ns at a constant pressure of 1 atm and 300 K using the *pmemd.cuda_SPFP* engine,[76] as implemented in AMBER 16 for GeForce Nvidia GTX 980 graphics processing units. Trajectory snapshots were collected every 0.1 ns for further analysis by means of the *cpptraj* module in AMBER.[77] Sets of coordinates taken every 5 ns were cooled down from 300 to 273 K over a 1 ns period. The geometries of these "frozen" complexes were then optimized by carrying out an energy minimization until the root-mean-square of the Cartesian elements of the gradient was less than 0.01 kcal $mol^{-1}$ $Å^{-1}$. The resulting ensemble of 50 low-energy and geometrically optimized representative structures was used to calculate the residue-based, solvent-corrected interaction energies by means of our in-house MM-ISMSA program.[78] See also Figure S2 and Video 1.

## Biochemistry

The binding of ligands to cross-linked MT was evaluated by isolating the stabilized polymer by centrifugation, extracting the pellet, and analyzing the extracted bound ligands by HPLC. The reaction mixtures with the desired concentrations of ligands and cross-linked MT were equilibrated at the desired temperature for 30 min and centrifuged for 10 min at 50,000 rpm in a prewarmed Beckman TL120.2 rotor. The cross-linked MT pellets were resuspended in 1.0 mL of 10 mM phosphate buffer (pH 7.0), and the tubulin concentration was determined spectrofluorometrically.[79] Ten μM PTX was added to the pellets and to the supernatants as an internal standard, which were extracted 3 times with 1.0 mL of $CH_2Cl_2$. This procedure quantitatively separates the drugs, which enter the organic phase, from the tubulin, which precipitates at the organic-aqueous interface. After evaporation of the $CH_2Cl_2$, the residues were each dissolved in 100 μL of 70% (v/v) methanol. HPLC analysis was performed on a C-18 column (Agilent ZORBAX Eclipse XBD-C18 150 × 4.6 mm, 5 mm bead size) developed isocratically with 70% methanol (LAU analogs), 60% methanol (PLA analogs) or in two steps 60% and then 70% to separate PLA analogs from LAU ones in competition experiments at a flow rate of 1.0 mL/min followed at 205 nm. Drug concentrations in the pellet were determined by integration of eluted peaks in comparison to the areas produced by the internal standard.

Polymerization of 25 μM tubulin in PEDTA buffer (10 mM sodium phosphate (NaPi), 1 mM EDTA, 1 mM GTP, 7 mM $MgCl_2$) or GAB buffer (10 mM sodium phosphate (NaPi), 3.4 M glycerol, 1 mM EDTA, 1 mM GTP, 6 mM $MgCl_2$) was monitored in the presence of 27.5 μM ligand by turbidity at 350 nm, employing a Thermo Appliskan plate reader (Thermo Fisher, Waltham, MA, USA). Critical concentration of purified tubulin in GAB was measured as described in.[50] In brief, samples of 200 μL of 25 μM tubulin were incubated 45 min at 37°C in the presence of 27.5 μM of tested compound to reach polymerization equilibrium. Samples were then centrifuged at 100,000 g, 37°C for 20 min in a Beckman OptimaTM centrifuge, employing a TLA-100 rotor. Supernatants were separated from pellets, and these were resuspended in 200 μL of 10 mM NaPi pH 7.0, 1% SDS. Both supernatants and pellets were diluted 1/5 in 10 mM NaPi pH 7.0, 1% SDS buffer and protein concentration was determined by fluorimetry at $\lambda_{exc}$ = 220 nm and $\lambda_{em}$ = 323 nm. Protein concentrations at the supernatants correspond to the critical concentration ($C_r$) of tubulin, below which no significant formation of MTs occurs at a given experimental condition. See also Tables S2 and S3.

## Cell biology

Antiproliferation assays were performed as described.[50] $IC_{50}$ values were obtained by fitting the experimental data to a four-parameter logistic curve using SigmaPlot 14.5 software package (Systat Software, Inc., San Jose, CA, USA).

Indirect immunofluorescence images were obtained using A549 cells plated at a density of 50,000 cells/mL onto a 18 mm round coverslip, cultured overnight and treated with increasing amounts of the ligands or drug vehicle (DMSO) for 24 h. DMSO was always less than 0.5%. Cells were permeabilized using Triton X-100 and fixed with 3.7% formaldehyde as previously described.[80] Cells were

incubated with a DM1A monoclonal antibody reacting with α-tubulin. After that, samples were washed, incubated with FITC goat anti-mouse antibody and 3 μM DAPI (Merck) was added to stain chromatin. The slides were examined with a Leica DM 6000 B epi-fluorescence microscope employing a 100× objective with a N.A. of 1.46 and images were recorded using a Leica DFC360 FX CCD camera. See also Table S3.

### Crystallization and crystal structure determination

For the $T_2R$-TTL complex, tubulin (8 mg/mL), TTL (17 mg/mL) and RB3 (26 mg/mL) were mixed at 2:1:1 ratio and concentrated (Amicon MWCO 10) at 4°C to a final complex concentration of 20 mg/mL. The concentrated mixture was supplemented with 10 mM DTT, 0.1 mM GDP and 1 mM AMPCPP before setting crstallization experiments. Initial crystallization conditions were determined from previous structures[26] using the sitting-drop vapour diffusion technique with a reservoir volume of 200 μL and a drop volume of 1 μL of complex and 1 μL of reservoir solution at 20°C. Crystals-producing conditions were further optimized using the hanging drop vapor diffusion method with a reservoir volume of 500 μL and a drop volume of 1 μL of complex and 1 μL of reservoir solution. Native $T_2R$-TTL complex was crystallized in 0.1 M Mes/0.1 M imidazole pH 6.7, 0.03 M $CaCl_2$, 0.03 M $MgCl_2$, 5 mM L-tyrosine, 11% glycerol, 10% PEG4000 for the CW1 complex or 0.1 M Mes/0.1 M imidazole pH 6.5, 0.03 M $CaCl_2$, 0.03 M $MgCl_2$, 5 mM L-tyrosine, 5% glycerol, 5.5% PEG4000 for the PPH complex. Plates were kept at 20°C and crystals appeared within the next 24 hours. Crystals were soaked with 2 mM of CW1 or 10 mM of PPH. Prior flash-cooling in liquid nitrogen, crystals were cryo-protected using 10% PEG4000 and increasing glycerol concentrations (16% and 20%). X-ray diffraction data were collected on beamline X06DA at the Swiss Light Source (Paul Scherrer Institute, Villigen PSI, Switzerland) and beamline ID30B at European Synchrotron Light Source (ESRF, Grenoble, France). Diffraction intensities were indexed and integrated using XDS,[81] and scaled using XCALE[81] (CW190) or AIMLESS[82] (PPH). The structure of CW190 was determined by the difference Fourier method in PHENIX[83] using PDB code 5lxt as starting model. The structure of PPH was solved by molecular replacement in PHASER[84] using the previously determined structure (PDB: 4o2b) as a search model. Structures were completed with cycles of manual building in COOT[85] and refinement in PHENIX.[83] PDB: 8a0l, 7zx2 (CW190 and PPH, respectively).

### QUANTIFICATION AND STATISTICAL ANALYSIS

MT structural features obtained from fiber diffraction images are represented as mean ± SE from 24 images as described in.[25] In brief, the standard error of the calculated values corresponding to the equatorial profiles was determined from the ratio between the experimental maximum intensities' values of $J_0$ and $J_n$ and their standard deviation. The standard error of the average monomer lengths was obtained from the standard deviation of the regression applied.

Temperature dependence and thermodynamical parameters of LAU binding to MTX are represented as mean of the natural logarithm of the binding constant ± SE of triplicated experiments.

Biochemical and cytotoxic parameters are represented as mean ± SE of triplicated experiments.

Data collection and refinement statistics are summarized in Table S4.